

Seismicity During the Initial Stages of the Guy-Greenbrier, Arkansas, Earthquake Sequence

Clara E. Yoon¹, Yihe Huang^{1,2}, William L. Ellsworth¹, and Gregory C. Beroza¹

¹Department of Geophysics, Stanford University, Stanford, California, USA.

²Department of Earth and Environmental Sciences, University of Michigan, Ann Arbor, Michigan, USA.

Key Points:

- We detected and located microearthquakes from first 3 months of the Guy-Greenbrier sequence in 2010 with a sparse 3-station seismic network
- Most events ($-1.5 \leq M_L \leq 2.9$) in June to September 2010 were induced by hydraulic fracturing at some but not all stimulated wells
- Initial seismic activity on the Guy-Greenbrier Fault was induced by wastewater injection starting in July 2010

This is the author manuscript accepted for publication and has undergone full peer review but has not been through the copyediting, typesetting, pagination and proofreading process, which may lead to differences between this version and the [Version of Record](#). Please cite this article as doi: [10.1002/2017JB014946](https://doi.org/10.1002/2017JB014946)

Corresponding author: Clara E. Yoon, ceyoon@stanford.edu

Abstract

We analyze the background seismicity, initiation, and earliest stages of the Guy-Greenbrier, Arkansas, earthquake sequence, which was potentially induced by wastewater injection starting in July 2010, during the 3-month time period 2010-06-01 to 2010-09-01. High-resolution observations of low-magnitude seismicity, and the high-quality Arkansas public well database, facilitate detailed analysis of spatial and temporal correlations between earthquakes, wastewater injection, and hydraulic fracturing. We detected 14,604 earthquakes, with magnitudes $-1.5 \leq M_L \leq 2.9$, using two sensitive, waveform-similarity-based event detection methods in parallel: Fingerprint And Similarity Thresholding (FAST), and template matching. We located the 1,740 largest earthquakes that form 16 spatially compact clusters, using P and S phases from 3 stations with the double-difference relocation algorithm and an improved velocity model constrained by the location of quarry blasts. We enhanced the temporal resolution of these event clusters by assigning smaller unlocated events to a cluster based on waveform similarity. Most clustered earthquakes during this time were both spatially and temporally correlated with hydraulic fracturing stimulation at several production wells. For one cluster, microseismicity was correlated with individual stages of stimulation. Many other wells had no detectable nearby seismicity during stimulation. We found a smaller number of events located on the Guy-Greenbrier Fault that were likely induced by wastewater injection. The concurrent presence of seismicity induced by hydraulic fracturing and wastewater injection presents a challenge for attribution and seismic hazard characterization, but the combination of precision seismology and high-quality well information allows us to disentangle the effects of these two processes.

1 Introduction

Since 2009, the central and eastern United States, an intraplate region with historically low levels of seismicity, has experienced a striking increase in earthquake activity, including several damaging earthquakes greater than magnitude 5 [Ellsworth *et al.*, 2013; Rubinstein and Mahani, 2015]. Many of these earthquakes, especially the larger ones, are thought to have been induced by deep injection of large volumes of wastewater produced by oil and gas operations over several years [Ellsworth *et al.*, 2013; Rubinstein and Mahani, 2015; Walters *et al.*, 2015]. Increased pore fluid pressure from injection can reduce the effective normal stress across a preexisting fault close to failure, unclamping it and allowing it to slip [Healy *et al.*, 1968; Raleigh *et al.*, 1976]. The Guy-Greenbrier area in central Arkansas (Figure 1), where hydraulic fracturing was used to increase natural gas production in the Fayetteville Shale, experienced several moderate strike-slip earthquakes: M_w 4.0 in October 2010, then M_w 4.1 on 2011-02-19, and finally the largest earthquake with M_w

45 4.7 (yellow star) on 2011-02-27 [Horton, 2012]. These earthquakes were part of an intense sequence
46 that lasted over a year. They were reported to start in July 2010 following injection of wastewater at
47 Well 1 (Figure 1, inverted triangle), and migrated southwest over the next few months, illuminating
48 a previously unknown ~13-km long, near-vertical fault with strike ~N30°E, subsequently named the
49 Guy-Greenbrier Fault for the nearby towns [Horton, 2012]. After the M_w 4.7 earthquake, injection
50 stopped at the wells nearest the fault in March 2011 on an emergency order from the Arkansas Oil
51 and Gas Commission (AOGC) [Horton, 2012]. The seismicity promptly decreased but remained
52 higher than the background seismicity rate before the sequence for at least the next 7 months [Huang
53 and Beroza, 2015].

54 We perform a retrospective analysis to understand how the Guy-Greenbrier earthquake sequence
55 initiated, and to determine whether it was induced by wastewater injection. *Ogwari et al.* [2016]
56 detected and located earthquakes in the first 4 months of the sequence, starting from the onset of
57 wastewater injection at Well 1 on 2010-07-07, to 2010-10-20. Their improved catalog, complete
58 down to M 0.2 and containing events down to M -0.6, revealed seismicity that started in the shallow
59 (2-4 km depth) sedimentary formation below injection Well 1, and migrated southwest and down into
60 the basement (deeper than 4 km) from September to October 2010. However, *Ogwari et al.* [2016]
61 found only scattered seismicity without any particular spatial or temporal characteristics during the
62 time immediately following injection, from 2010-07-07 to the end of August 2010. We chose to study
63 the 3-month time period from 2010-06-01 to 2010-09-01. This includes the month before injection
64 started at Well 1, which should help us understand background seismicity in the region, as well as the
65 two months right after the start of injection, so that we can characterize the earliest stages of seismicity
66 occurring in response to injection. The Advanced National Seismic System (ANSS) catalog contains
67 only 75 events during these 3 months (Data Set S1), with uncertain locations, and few of them near
68 the soon-to-be activated Guy-Greenbrier Fault (Figure S1). Similar off-fault locations were seen for
69 events located with the regional Cooperative New Madrid Seismic Network (CNMSN) during this
70 time [Horton, 2012]. We detect and locate as many small earthquakes as possible from continuous
71 seismic data for these 3 months using a sparse 3-station network (Figure 1, black triangles), then
72 explore spatial and temporal correlations between the seismicity and unconventional hydrocarbon
73 development.

74 We also consider the possibility that earthquakes in the Guy-Greenbrier sequence may have
75 been induced by hydraulic fracturing itself, instead of deep disposal of the by-product wastewater.
76 Hydraulic fracturing injects fluids at high pressure in order to increase natural gas production at wells
77 that are oriented horizontally within the target rock formation. This process creates small fractures

78 in the formation, increasing its permeability and facilitating flow of the natural gas [Davies *et al.*,
79 2013; Rubinstein and Mahani, 2015]. In a process called stimulation, fluid injection is carried out
80 in stages along different sections on the horizontal section of the production well, over a period of
81 several days. The first stage is usually located near the toe (furthest point) of the well and subsequent
82 stages move progressively back to the heel (where the well turns from horizontal to vertical). In each
83 stage, which typically lasts several hours, a slurry containing a mixture of fluid and solid proppant is
84 injected at a pressure high enough to fracture the rock, overcoming the minimum compressive stress.
85 In hydraulic fracturing, the volume and duration of fluid injection are lower, but the pressure is much
86 higher, compared to wastewater disposal; therefore, they have different potential risks for inducing
87 earthquakes [Walters *et al.*, 2015]. Hydraulic fracturing is expected to generate microearthquakes
88 with magnitude $-3 < M < 0$, since the intent is to create fractures restricted to the target formation
89 [Warpinski *et al.*, 2012; Maxwell, 2013; Rubinstein and Mahani, 2015]; however, several studies
90 have reported the occurrence of $M > 1$ earthquakes induced by hydraulic fracturing in Oklahoma
91 [Holland, 2013], Ohio [Friberg *et al.*, 2014; Skoumal *et al.*, 2015a,b], United Kingdom [Clarke *et al.*,
92 2014], and western Canada, in northeast British Columbia and northwest Alberta [BCOGC, 2012,
93 2014; Farahbod *et al.*, 2015; Schultz *et al.*, 2015a,b, 2016; Atkinson *et al.*, 2016; Bao and Eaton,
94 2016; Wang *et al.*, 2016], including a M 4.6 event in British Columbia [Atkinson *et al.*, 2016]. These
95 events are likely caused by reactivation of nearby critically stressed faults that are well-oriented to
96 slip in the local stress field [Maxwell, 2013]. Ogwari *et al.* [2016] found a cluster of seismicity west
97 of the Guy-Greenbrier Fault that was probably induced by hydraulic fracturing from 2010-09-29
98 to 2010-10-04. We search for spatial and temporal correlations between seismicity and the many
99 production wells with hydraulic fracturing stimulation (Figure 1, small red-orange triangles with
100 black lines) during 2010-06-01 to 2010-09-01.

101 **2 Methods and Results**

102 **2.1 Data**

103 The permanent seismic network in Arkansas is sparse, but includes a 3-component broadband
104 seismic station WHAR (Figure 1, black triangle) recording 100 Hz data continuously since May
105 2010, located close to the Guy-Greenbrier Fault and in the area being prepared for production
106 [Horton, 2012; Ogwari *et al.*, 2016]. ARK1 and ARK2, two temporary 3-component stations that
107 started recording on 2010-06-11, were the only other available local seismic stations operating during
108 2010-06-01 to 2010-09-01; they are also known as CH1 and CH2 [Ogwari *et al.*, 2016; Mousavi *et al.*,
109 2017] or CHKGRS and CHKGUY [Huang *et al.*, 2016], respectively. We first detect earthquakes on

110 the single station WHAR, then use data from all 3 stations to confirm these detections and to locate
111 and estimate magnitudes of the newly detected earthquakes.

112 2.2 Earthquake detection

113 To characterize fully the beginning stages of the Guy-Greenbrier earthquake sequence, we first
114 detect as many earthquakes as possible. *Huang and Beroza* [2015] used single-station template
115 matching on WHAR to detect up to 100 times more earthquakes than were recorded in the ANSS
116 catalog between June 2010 and October 2011 in this earthquake sequence. Template matching,
117 which cross-correlates known catalog template waveforms with continuous data to detect previously
118 unknown low-magnitude events, exploits waveform similarity to improve detection sensitivity, and
119 has often been used to resolve details of induced seismicity [e.g., *Holland*, 2013; *Friberg et al.*, 2014;
120 *Skoumal et al.*, 2015a,b; *Schultz et al.*, 2015a,b, 2016].

121 The Fingerprint And Similarity Thresholding (FAST) earthquake detection method [*Yoon et al.*,
122 2015] adapts data-mining algorithms to perform a comprehensive search for similar earthquake
123 waveforms within long duration continuous seismic data. It is especially useful in situations where
124 template waveforms are not available or are not representative of all earthquake sources in an area.
125 FAST assumes that every time window in continuous data is a potential template, and searches for
126 time windows with similar waveforms in a computationally efficient way. FAST trades off speed for
127 accuracy: instead of directly comparing waveforms, it computes fingerprints that replace waveforms
128 with key discriminative features, and compares fingerprints for similarity in a probabilistic manner.

129 We use FAST with parameters in Table S1 to detect earthquakes in continuous data from station
130 WHAR, bandpass filtered from 1-20 Hz, during the 3-month study period 2010-06-01 to 2010-09-01.
131 First, we ran the single-channel detection algorithm in *Yoon et al.* [2015] independently on each
132 component of data at WHAR. The runtime was about 5 days per component on a single processor.
133 The output of FAST on a single component, which we can view as a sparse matrix (Figure 2), is a list
134 of pairs of times within the continuous data with their associated FAST similarity score, where the
135 fingerprints (and therefore waveforms) are similar. Earthquake signals should maintain similarity
136 in time on all 3 components, so we expect the FAST similarity to add coherently at times when
137 similar earthquakes occur. We sum the FAST similarity matrix from each component to get the
138 total 3-component FAST similarity, on which we empirically set an event detection threshold of 0.33
139 by inspection (Table S1). After removing near-duplicate pairs and events within 4 s (Table S1) as
140 described in *Yoon et al.* [2015], we find 28,675 events above this threshold.

141 FAST also detects non-earthquake signals with similar waveforms, so we need to remove these
142 during post-processing. This is less of a concern for template matching, which only finds matches to a
143 known earthquake waveform. Many of the similar non-earthquake signals are extremely narrowband
144 (Figure S2), and we classify them as noise if they exceed the empirically determined threshold where
145 at least 56% percent of the total signal power is within 1.5 Hz of the peak frequency on any one
146 component. After removing 10,738 events classified as narrowband noise, we visually inspect the
147 remaining 17,937 events and retain only the 13,026 events with a clear earthquake signal (containing
148 P, S, and coda waves), preferably on at least two stations: WHAR and ARK2 or ARK1 (Figure 1,
149 black triangles).

150 We compare the detection performance of FAST against that of template matching from *Huang*
151 *and Beroza* [2015] during the 3-month study period. Templates, taken from ANSS catalog event
152 waveforms at WHAR between May and October 2010, were 4 seconds long and bandpass filtered
153 from 1-20 Hz. These templates were cross-correlated with continuous data at WHAR every 0.05
154 seconds. A different correlation coefficient (CC) threshold was used for each template, and for each
155 hour of data. Event detection for template matching requires exceeding a CC threshold of 8 times the
156 median absolute deviation. FAST detects a total of 13,026 events, while template matching found
157 13,946 events; most (12,368) events are detected by both methods (Figure 3, blue). In contrast, the
158 ANSS catalog has only 75 events during this time (Data Set S1). Template matching detected 74
159 out of 75 catalog events; the remaining catalog event was not detected because it happened during a
160 time gap in the continuous data at WHAR. FAST detected only 55 out of 75 catalog events, which
161 suggests that the fingerprints may be less similar for the larger events, emphasizing the value of
162 applying multiple detectors.

163 Figure 3 shows the local magnitude M_L (Section 2.3) as a function of time for all 14,604 events
164 detected by either FAST, template matching, or both methods (Data Set S2). These events are
165 microearthquakes, with the largest magnitude $M_L \leq 2.9$. FAST detects an additional 658 events that
166 template matching did not find (Figure 3, cyan), which are lower in magnitude and clustered in time,
167 demonstrating that a comprehensive search for similar earthquakes in continuous data finds unknown
168 small events that would otherwise be overlooked. On the other hand, template matching found more
169 (1,578) events that FAST fails to detect (Figure 3, magenta), which are lower in magnitude than most
170 events but more evenly distributed in time. FAST is unable to detect every single event because it
171 makes approximations in both representing waveforms and in searching for similar waveforms, but
172 this tradeoff allows us to search thoroughly and efficiently a 3-month continuous seismic data set,

173 and still find 13,026/14,604 \approx 89% of all detected events. Template matching successfully captures
174 most small earthquakes (13,946/14,604 \approx 95% of all detected events) in this data set.

175 **2.3 Magnitude estimation**

176 We estimate local magnitude M_L for all 14,604 detected events, which ranges from -1.5 to
177 2.9 (details in Section S1). In order to calibrate the M_L estimate, we first calculate the moment
178 magnitude M_w for a selected group of 54 larger events with high-quality waveforms, located at
179 different distances from station WHAR (Figure S3a). We obtain M_w by calculating seismic moment
180 in the time domain from displacement waveforms at WHAR [Prejean and Ellsworth, 2001]. Next,
181 we measure peak amplitudes on horizontal-component Wood-Anderson seismograms at all 3 stations
182 for these 54 events, and invert for the distance correction parameters in the M_L estimate (Figure S3b).
183 Finally, we apply this distance correction to peak Wood-Anderson amplitudes for all detected events
184 to determine M_L [Bormann, 2012]. For the ANSS catalog events, the catalog magnitudes M_d
185 computed from the coda duration are reasonably consistent with our M_L values (Figure S4a).

186 **2.4 Initial earthquake location and refined velocity model**

187 First, we determine absolute locations for 1,229 events with high-quality P and S phase arrivals
188 on all 3 stations (Section S2). We estimate locations with VELEST [Kissling *et al.*, 1994] using
189 the 1D velocity model from Ogwari *et al.* [2016], which was itself derived using VELEST as an
190 improvement over the original 1D velocity model for this area [Chiu *et al.*, 1984].

191 Three of our events, all located near each other, have similar waveforms with high-amplitude
192 surface waves characteristic of quarry blast sources [Kafka, 1990]. They occurred on 2010-06-24,
193 2010-07-02, and 2010-08-10 (Figure 4a). These events were detected by template matching but
194 missed by FAST because the fingerprints of their waveforms at WHAR were not highly similar.
195 Google Maps shows that the Greenbrier Quarry, owned by Rogers Group Inc., is located 1-2 km
196 from our initial locations for these events. Inspection of Google Earth satellite imagery near the
197 quarry location before (2009-07-23) and after (2010-09-15) the quarry blast times (Figure 4b) reveals
198 a notch (red circle) in the southeast corner of the quarry in the post-blast image that was not in the
199 pre-blast image. We therefore infer that all three blasts occurred on the surface (depth 0 km) at this
200 notch location: 35.2928° N, 92.3973° W.

201 We use the notch location as ground truth for the 3 quarry blasts and solve for an updated 1D
202 velocity model in VELEST, starting with the Ogwari *et al.* [2016] velocity model (Section S3). Table

1 lists the resulting improved 1D velocity model constrained by the quarry blast location; the V_p/V_s ratio deviates significantly from $\sqrt{3}$. Figure 5, which compares the new velocity model (solid lines) against the starting *Ogwari et al.* [2016] model (dashed lines), shows that the new model is slower at shallow depths where most events are located. We calculated this new model in order to refine velocity estimates in the shallowest layers within this small local area. We do not necessarily intend this model to replace the *Ogwari et al.* [2016] velocity model for the entire CNMSN.

We use the new velocity model (Table 1) to locate the events again in VELEST, starting with the same initial hypocenter location for all 1,229 events (1,226 earthquakes and 3 quarry blasts), equally weighting P and S travel times, and completing 50 iterations. Free locations of the 3 quarry blasts (Figure 1, nearby red circles) differ from the actual quarry location (Figure 1, red diamond) by as much as 2 km, which indicates a remaining absolute location error. Using the new quarry-constrained velocity model, the total root-mean-square (rms) residual for the 1,229 VELEST-located events is 0.0306, which is lower than the residual of 0.0347 for the *Ogwari et al.* [2016] velocity model.

We do not use the *Chiu et al.* [1984] velocity model for two reasons. First, the total rms residual from the resulting earthquake locations is higher than that from the *Ogwari et al.* [2016] model. Second, earthquake locations from the *Chiu et al.* [1984] model at the north end of the Guy-Greenbrier Fault in Box B1 (Figure 1) are inconsistent with the back-azimuth of these events calculated from P-wave polarization analysis [*Havskov and Ottemoller, 2010*] at station ARK2 (Figure S5).

2.5 High-precision earthquake location

The 1,229 events located by VELEST form several spatially compact clusters (Figure 1). To resolve the internal structure of each cluster, we use double-difference earthquake relocation [*Waldhauser and Ellsworth, 2000*], specifically hypoDD version 2.1b that allows as input the 1D quarry-constrained velocity model (Table 1) with variable V_p/V_s ratios in different layers.

We first compute differential travel times from both catalog P and S picks and cross-correlation for the 1,229 events where we already have initial absolute locations from VELEST (Section S4). We then compute cross-correlation differential times between each of the 1,229 initially located events and the 13,375 remaining unlocated events, which allows us to locate 511 additional events. Although these remaining events lack enough reliable P and S picks to locate with VELEST, their source locations are near already-located events such that the cross-correlation of time windows from the located and unlocated events will yield reliable relative locations in hypoDD.

234 We obtain precise relative earthquake locations within each cluster by running hypoDD in
 235 LSQR mode with parameters from Table S3 and weights from Table S4, using 904,354 *P* and
 236 1,567,757 *S* cross-correlation differential travel times, as well as 72,368 *P* and 72,310 *S* catalog
 237 differential travel times. The blue bars in Figure 6 display the magnitude-frequency distribution of
 238 all 1,740 located events. 1,719 out of 1,740 events belong to one of 16 spatially compact clusters of
 239 earthquakes as defined by the latitude and longitude boundaries listed in Table S5. Figure 1 plots
 240 these event locations as circles sized by relative magnitude and colored by depth. Most of the events
 241 are located on or near the Guy-Greenbrier Fault. Profile A-A', a depth slice along the ~N30°E strike
 242 of the Guy-Greenbrier Fault [Horton, 2012; Ogwari *et al.*, 2016], shows only events located within
 243 0.5 km of the fault; most events occur at the northeastern end in distinct clusters with relatively
 244 shallow depth (2-4 km), while there is a deeper (4-6 km depth) cluster of events to the southwest. In
 245 subsequent figures, Boxes B1 and B2 (red rectangles) explore 5 event clusters along or near the fault
 246 in greater detail. In addition, a significant number of events, many of them in compact clusters, are
 247 located at least 4 km away from the Guy-Greenbrier Fault. Profile B-B', a depth slice normal to the
 248 Guy-Greenbrier Fault, indicates not only the circled events along the near-vertical Guy-Greenbrier
 249 Fault, but also several event clusters located off the main Guy-Greenbrier Fault. In later figures, Box
 250 B3 (red rectangle) zooms in on 5 off-fault event clusters to the southeast, while Boxes B4 and B5
 251 (red rectangles) closely examine 3 off-fault event clusters to the northwest. The map in Figure 1
 252 also shows the location of 3 isolated earthquake clusters (C14, C15, C16 in blue boxes). To estimate
 253 the relative location error between pairs of closely spaced events, we run hypoDD in singular value
 254 decomposition (SVD) mode separately for 3 subsets of events: Cluster 3, Cluster 4, and Cluster
 255 11. The relative location uncertainty is < 10 m for events within a cluster, which suggests that the
 256 structure within each cluster is real.

257 **2.6 Improving temporal resolution of seismicity**

258 Double-difference relocation significantly improves the spatial resolution of the 1,740 located
 259 earthquakes (Data Set S3). We are unable to locate the majority (12,864/14,604 \approx 88%) of the
 260 detected events from Figure 3 because we lack quality *P* and *S* arrival picks at enough stations;
 261 however, we can improve the temporal resolution of the earthquake sequence by assigning unlocated
 262 events to Clusters 1-16 (Table S5) based on waveform similarity at station WHAR [Cattaneo *et al.*,
 263 1999]. Also, stations ARK1 and ARK2 did not start operating until 2010-06-11, so we can only
 264 assign, instead of locate, events that occurred before this date. We represent each cluster with a stack
 265 waveform at WHAR, generated by averaging all located events belonging to that cluster. We then

266 cross-correlate each unlocated event with the stack waveform from every cluster, and assign it to the
267 cluster with the highest CC. Section S5 has a detailed description of the assignment procedure.

268 Figure 7 verifies that the 2,525 unlocated events assigned to Cluster 1 have similar waveforms
269 to each other and to the 667 located events in this cluster (shaded orange) at the 3 components of
270 station WHAR. The CC between the pictured stack waveform (blue) and each of the 2,525 assigned
271 events was at least 0.5. In all clusters, the high degree of waveform similarity gives us confidence
272 that the assigned events originate from nearly the same source as the located events, and therefore
273 can reliably improve the temporal resolution of the cluster.

274 For all clusters, the assigned events provide important information about the lower-magnitude
275 events (Figure 6, black) and their timing within each cluster. The assigned events comprise
276 (6,508/14,604 \approx 44%) of the detected events, in addition to the (1,740/14,604 \approx 12%) located
277 events; however, 6,356 remaining detected events have waveforms that are too noisy to locate or
278 assign (Figure 6, red), which are predominantly at the lowest magnitudes. We do not know if they
279 are tiny events belonging to existing clusters, if they are events with different focal mechanisms in
280 the same cluster, or if they are distinct or more distant earthquake sources that produce only small
281 events.

282 **2.7 Spatial and temporal correlation of seismicity with well data**

283 Most of the 16 earthquake clusters are located near a production well stimulated by hydraulic
284 fracturing (Figure 1, small red-orange triangles with black lines) or a wastewater injection well
285 (Figure 1, inverted triangles), showing a spatial correlation. There are also many production wells
286 without any nearby seismicity, although many of these wells are located more than 10 km from
287 WHAR, so we would be less likely to detect seismicity near these wells, if it exists. We also check
288 for a temporal correlation between seismicity in each cluster and the start date of wastewater injection
289 at disposal wells, as well as the duration of stimulation stages at all production wells within a 2 km
290 radius of the cluster, considering the absolute event location uncertainty.

291 **2.7.1 Wastewater injection wells**

292 Table S7 lists all wastewater disposal wells within the map area in Figure 1 (inverted triangles
293 labeled by well number) active during the study period 2010-06-01 to 2010-09-01. Injection Wells 1
294 and 5 (colored by depth in Figure 1), which started injecting during the study period on 2010-07-07
295 and 2010-08-16 respectively, are the two injection wells located closest to the Guy-Greenbrier Fault.

296 The magnitude-time plots for located (blue) and assigned (black) events in each cluster (Figures 8,
297 13-15) show the start date of injection at Wells 1 and 5 as black dashed lines.

298 **2.7.2 Stimulated production wells**

299 Table S8 identifies all 53 production wells within the map area in Figure 1 (small triangles
300 with black lines, colored by their true vertical depth) stimulated during the study period 2010-06-01
301 to 2010-09-01. The triangle indicates the surface location of the well, while the line shows the
302 horizontal well path from heel to toe. We first queried the public Arkansas Oil and Gas Commission
303 well database [AOGC, 2017a] for all production wells in the three counties spanning our map area
304 (Faulkner, Cleburne, and Van Buren), then retained permit numbers for only the 53 wells inside
305 the map boundaries in Figure 1 that were stimulated during the study period. We then searched
306 the Arkansas Oil and Gas Commission Document Imaging Wells File Cabinet [AOGC, 2017b]
307 by permit number for detailed production well data, including precise horizontal well trajectories
308 and information about perforation and stages of hydraulic fracturing stimulation. The quality of
309 stimulation data available varies widely depending on the company that collected and submitted the
310 data. Some wells have detailed logs of the exact timing, injection rates, pressures, volumes, and
311 chemical composition of each fluid injection within every stage of stimulation, while other wells have
312 a short summary with only the start and end dates of stimulation. If timing information is available for
313 stimulation stages, we convert the stimulation times from local Arkansas time (Central Daylight Time)
314 to UTC time by adding 5 hours, for consistency with the seismic data. The magnitude-time plots for
315 located and assigned events in each cluster (Figures 8, 13-15) show the duration of stimulation at all
316 production wells within 2 km of the cluster (listed for each cluster in last column of Table S5) as a
317 purple box, spanning the time from the start of the first stage to the end of the last stage.

318 **2.7.3 Seismicity clusters near the Guy-Greenbrier Fault**

319 Figure 8 focuses on seismicity located on or near the Guy-Greenbrier Fault, within Clusters 1-5
320 (blue boxes) in Boxes 1 and 2 from Figure 1, along with nearby production wells (small triangles
321 with horizontal well path lines) and injection wells (inverted triangles). The magnitude-time plots
322 for located and assigned events in each cluster explore temporal correlations between injection,
323 stimulation, and the occurrence of seismicity.

324 Cluster 1, the northernmost cluster in Figure 8 located just northwest of the Guy-Greenbrier
325 Fault, is the largest cluster with 3,192 total events (667 located and 2,525 assigned, Table S5).

326 Most events in Cluster 1 are shallow, with depth 2-3 km. These events locate on three east-west
327 oriented structures, perpendicular to the north-south horizontal well path orientations of the 5 nearest
328 production wells overlapping this cluster on the map. In addition, the magnitude-time plot for Cluster
329 1 shows an abrupt increase in both located and assigned seismicity that closely coincides with the
330 timing and duration of stimulation (purple boxes) at the 7 nearest production wells in July 2010
331 (except for well 42069, which was stimulated in June 2010, and is temporally correlated with some
332 $M_L < 1$ events in Cluster 1), with the seismicity lasting for several weeks after the end of stimulation
333 before decaying with time. Cluster 1 is also located near injection Well 1 (about 3 km away), and
334 most events occur after injection began at Well 1 with a time delay of about a week, but the obvious
335 spatial and temporal correlations with the nearby stimulated production wells lead us to conclude that
336 Cluster 1 seismicity was likely induced by hydraulic fracturing, rather than by wastewater injection.

337 Cluster 1 had the highest quality data, including a large number of earthquake locations, several
338 stimulated production wells, and comprehensive stimulation data with start and stop times for all
339 stages at each well. This led us to a more detailed investigation of spatial and temporal correlations
340 between seismicity on different structures within Cluster 1 and each stage of stimulation at the 5
341 nearest production wells. Figure 9 examines the time evolution of Cluster 1 seismicity and stimulation
342 stages at the 5 nearest production wells (permit numbers 42146, 42389, 42262, 43344, 43343), which
343 are both colored by time with Day 0 defined as 2010-07-16 00:00:00 UTC. The event locations in
344 Figure 9a are slightly offset from the horizontal well paths, which we attribute to our 2 km absolute
345 location error resulting from the sparse 3-station network used for location. Figure 9b shows the
346 seismicity shifted ~ 0.7 km southeast relative to the Figure 9a locations, which now completely overlie
347 the 5 well paths, making it easier to view the detailed correlations where seismicity and stimulation
348 stages on particular well sections have matching colors. This is motivated by our knowledge that
349 relative location errors are much smaller and the geometry of locations is consistent with stimulation.
350 In addition, the shifted locations in Figure 9b, which are within the 2 km absolute location uncertainty,
351 agree with the back-azimuth derived from P-wave polarization analysis at station ARK2 (Figure S5).

352 Movie S1 displays the cumulative time evolution of Cluster 1 seismicity and stimulation stages
353 at production wells 42146, 42389, 42262, 43344, 43343, both colored by the number of days since
354 2010-07-16 00:00:00 UTC (defined as Day 0); shifted event locations from Figure 9b are plotted.
355 Figure 10a-d shows seismicity and stages during four different time intervals from Movie S1. The
356 first stimulation stage started at the toe of the easternmost well 43343, and stages alternated between
357 well 43343 and the adjacent well 43344 moving south during the first 3 days (red) in a zipperfrac
358 pattern [Vermylen and Zoback, 2011], with seismicity closely following (Figure 10a). Then on day

359 3 (orange), while stimulation continued on wells 43343 and 43344, stimulation started at the toe of
360 well 42389 to the west, and stages alternated between well 42389 and the adjacent westernmost well
361 42146 moving south toward the heel, again in a zipperfrac pattern, with seismicity also migrating in
362 the same direction (Figure 10b, c). On day 10 (cyan), stimulation started at the toe of the center well
363 42262, again moving north to south, and the seismicity predictably follows the stages (Figure 10d).
364 Seismicity persisted at the southeastern corner of Cluster 1 (Figure 10c,d) even after stimulations
365 near the heel of wells 43343 and 43344 finished. Figure 10e displays a magnitude-time plot of the
366 16-day stimulation time period examined in Figure 9, Figure 10a-d, and Movie S1, with stimulation
367 stages from each well plotted in a different color. The seismicity rate is higher during or immediately
368 following the stimulation stages, which have a short duration of a few hours each, while seismicity
369 tapers off during longer breaks between stimulation (during days 2-3, 9-10, and 14-16). Figure 9,
370 Figure 10, and Movie S1 demonstrate a compelling spatial and temporal correlation of seismicity in
371 Cluster 1 with individual stages of hydraulic fracturing stimulation.

372 Cluster 2 is located about 1 km north of the Guy-Greenbrier Fault, just south of Cluster 1
373 (Figure 8). It has a large number of events (1,078 total) located at a depth of 3-4 km. Most events
374 in Cluster 2 are located on a 0.75 km-long, east-west oriented structure similar to those in Cluster
375 1, which is nearly orthogonal to the north-south well paths of the 8 nearby production wells. In the
376 magnitude-time plot for Cluster 2, some earthquakes happen following stimulation at well 42069 in
377 June 2010 (Table S8). In July 2010, a few events follow the start of injection at Well 1 (located
378 just 1 km away), but the seismicity rate does not experience a large increase until the end of July,
379 following stimulation at the remaining 7 nearby production wells. Compared to Cluster 1, there is a
380 longer time delay between the onset of stimulation and the rapid increase in seismicity; most events
381 in Cluster 2 actually occur after stimulation has ended. Such time delays, longer than a week, have
382 been observed in other cases of hydraulic fracturing induced seismicity [*Schultz et al.*, 2015a, 2016].
383 The location, orientation, and timing of Cluster 2 seismicity suggest that these events were probably
384 induced by hydraulic fracturing, rather than by wastewater injection. However, we cannot completely
385 exclude the possibility that Cluster 2 was induced by wastewater injection, due to its depth, timing,
386 and proximity to Well 1.

387 Most seismicity in Cluster 3, the closest earthquake cluster to injection Well 1, is oriented
388 along the strike of the Guy-Greenbrier Fault (Figure 8), although there is a small east-west oriented
389 sub-cluster of events at the northern boundary of Cluster 3 (Cluster 3C from Table S5). Cluster 4,
390 located farther southwest away from the production wells, contains fewer events, also located on
391 the Guy-Greenbrier Fault. The magnitude-time plots show that seismic activity in Clusters 3 and 4

392 significantly increases following injection at Well 1, after a short 3-day time delay, but is not affected
393 much by stimulation later in July. These events have depth 3-4 km and have lower magnitude (mostly
394 $M_L < 1$) than events in Clusters 1 and 2. The abrupt increase in seismicity starting on 2010-08-29
395 was reported in *Ogwari et al.* [2016] as the beginning of the Guy-Greenbrier sequence, but we see a
396 lower level of microseismicity initiate and persist within a few days of injection. We conclude that
397 Cluster 3 and 4 events have a stronger spatial and temporal correlation with, and thus are more likely
398 to be induced by, wastewater injection at Well 1, rather than stimulation.

399 The presence of distinct east-west trending structures formed by Clusters 1, 2, and 3C motivated
400 us to explore the source mechanism of these events. We select 300 events from Cluster 1, 159 events
401 from Cluster 2, and 22 events from Cluster 3C (Figure 11a) and plot their first motions (black "u":
402 up, red "d": down) on a composite focal mechanism projected onto the lower hemisphere (Figure
403 11b). Since we have sparse station coverage, we assume that all 3 clusters have the same mechanism.
404 Cluster 1 events are shifted ~ 0.7 km southeast as in Figure 9b for the first motion calculation. If we
405 assume a double-couple source mechanism, we can manually fit two nodal planes to the first motion
406 data, one trending $\sim N75^\circ E$ and the other oriented $\sim N15^\circ W$ (Figure 11b, black lines). If the $\sim N75^\circ E$
407 nodal plane is the fault plane, which is a reasonable assumption given the east-west orientation of
408 seismicity, the first motions indicate right-lateral strike-slip motion along this fault. However, given
409 the regional $\sim N60^\circ E$ maximum horizontal stress orientation [*Hurd and Zoback, 2012*], we would
410 expect left-lateral strike-slip motion along east-west oriented faults. Local heterogeneity in the stress
411 orientation is unlikely because the regional $\sim N60^\circ E$ stress orientation is consistent with right-lateral
412 strike-slip motion on the nearby favorably oriented $\sim N30^\circ E$ Guy-Greenbrier Fault [*Horton, 2012*].
413 This contradiction between the expected left-lateral slip from the stress orientation, and the observed
414 right-lateral motion on the focal mechanism, rules out the possibility that these events in Clusters 1,
415 2, and 3C are left-lateral strike-slip earthquakes activated on preexisting east-west faults favorably
416 oriented in the regional stress field [*Maxwell, 2013*]. Instead, we relax the double-couple assumption,
417 and suggest that these events have a combination of shear and tensile faulting. Although the sparse
418 data are inconclusive, the restricted region of dilatational first motions near the center of the focal
419 sphere (Figure 11b, red "d") could be explained by a non-double-couple mechanism with a volumetric
420 component resulting from opening of small east-west-oriented fractures [*Sileny et al., 2009; Fischer
421 and Guest, 2011; Vavrycuk, 2011*], which is an intended goal of hydraulic fracturing to facilitate
422 flow of hydrocarbons. The east-west seismicity is oriented perpendicular to the well paths, which
423 supports this idea, although there are several events in Cluster 1 with $M_L > 2$ (Figure 8), which is
424 higher than the expected $-3 < M < 0$ magnitude range of microseismicity from opening hydraulic

425 fractures [Warpinski *et al.*, 2012; Rubinstein and Mahani, 2015]. We note that our interpretation
 426 is limited by the lack of first motion data at enough stations, and it is possible that these 3 clusters
 427 actually have different mechanisms, contrary to our assumption.

428 Cluster 5 is located farther to the southwest on the Guy-Greenbrier Fault (Figure 8), in Box 2
 429 (Figure 1). These events align with the strike of the Guy-Greenbrier Fault and have depths around 5
 430 km. They are deeper than events in Clusters 1-4 farther northeast along the fault and were reported
 431 by *Ogwari et al.* [2016] as the first four events on the southern section of the fault. Cluster 5 was
 432 definitely not induced by injection at nearby Well 5, because most events occurred before the start
 433 of injection. There are two stimulated production wells near Cluster 5, and most of the events occur
 434 after stimulation at well 43114, so it is possible that Cluster 5 was induced by stimulation; however,
 435 the along-strike orientation, deeper depth, and lower seismicity rate (compared to Clusters 1 and 2,
 436 which were likely induced by hydraulic fracturing) suggest an alternative explanation that we favor:
 437 Cluster 5 could have been triggered by diffusion of pore pressure from injection at Well 1, with a
 438 longer time delay between the start of injection and the first event in August 2010.

439 Figure 12 summarizes all seismicity in Clusters 1-5 with epicenters restricted to within 0.5 km
 440 of the Guy-Greenbrier Fault (Profile A-A', Figure 1). Figure 12a shows the depth of these events
 441 as a function of along-strike distance (also shown in Figure 1), along with the location and depth
 442 (magenta sections) of wastewater injection Wells 1 and 5. It also displays the depths of the target
 443 Fayetteville Shale formation, the sedimentary Paleozoic Boone Formation/Ozark Aquifer into where
 444 injection occurs, and the crystalline Precambrian basement below [Ogwari *et al.*, 2016]. Since
 445 seismicity along the Guy-Greenbrier Fault is located within the triangular area outlined by the three
 446 seismic stations (Figure 1), these event depths should be reliable. Figure 12b shows the timing of
 447 events, as well as the onset of injection at Wells 1 and 5, along the strike of the Guy-Greenbrier
 448 Fault; it is obvious that Cluster 5 events occur before injection started at Well 5. We separate out the
 449 events in Clusters 1 and 2 (blue boxes labeled C1, C2) because they were likely induced by hydraulic
 450 fracturing stimulation. *Ogwari et al.* [2016] and *Mousavi et al.* [2017] report high b-values in these
 451 areas later on in September and October 2010, which is also consistent with hydraulic fracturing
 452 induced seismicity. The remaining events along the fault, belonging to Clusters 3, 4, 5, were probably
 453 induced by wastewater injection at Well 1. We estimate an apparent hydraulic diffusivity of $D \approx 1$
 454 m^2/s , assuming a homogeneous and isotropic medium [Shapiro *et al.*, 2002; Shapiro and Dinske,
 455 2009]:

$$r = \sqrt{4\pi Dt}. \quad (1)$$

456 Pore pressure diffuses outward from injection at Well 1, and reaches injection Well 5, located $r = 5.5$
457 km away, $t = 28$ days after injection started at Well 1. In comparison, *Ogwari and Horton* [2016]
458 used a detailed numerical model and observed seismicity to estimate hydraulic diffusivity along the
459 Guy-Greenbrier Fault during October and November 2010, when seismicity dramatically increased.
460 They found $D \approx 0.2\text{-}0.3$ m²/s in the northern and central sections of the fault (near Clusters 3 and
461 4), while in the southern section (near Cluster 5), their diffusivity was $D \approx 1.1$ m²/s above 5 km
462 depth and $D \approx 0.02$ m²/s below 5 km. *Mousavi et al.* [2017] estimated a lower hydraulic diffusivity
463 of $D \approx 0.01$ m²/s in the northern section of the Guy-Greenbrier Fault, from fitting Equation 1 to a
464 detailed catalog of seismicity from *Ogwari et al.* [2016] during the time period from 2010-07-07
465 to 2010-10-20, following injection at Well 1. The results in Figure 12 foreshadow the migration of
466 seismicity from northeast to southwest and from the shallower Paleozoic sedimentary formation into
467 deeper Precambrian basement seen soon afterward in September-October 2010 [*Ogwari et al.*, 2016;
468 *Ogwari and Horton*, 2016].

469 **2.7.4 Seismicity clusters off the Guy-Greenbrier Fault**

470 Figure 13 takes a closer look at seismicity located 5-10 km southeast of the Guy-Greenbrier
471 Fault, within Clusters 6-10 (blue boxes) in Box 3 from Figure 1, and nearby production wells that were
472 stimulated during 2010-06-01 to 2010-09-01. Magnitude-time plots for located and assigned events
473 in each cluster examine temporal correlations between injection at Wells 1 and 5, stimulation, and
474 the occurrence of seismicity. Since these events are located outside the 3-station network, their depth
475 estimates are unreliable. We ended up with greater (4-8 km) depth estimates than those from ANSS
476 catalog events in this area (Figure S1), although the depths mostly agree within the large uncertainties
477 in the catalog depths (Figure S4b). Cluster 6 contains events in an east-west orientation, and there
478 is an obvious temporal correlation between seismicity and the duration of stimulation at the nearest
479 production well 43043. The first detected and associated (not located) event starts about 3 hours
480 after the onset of the first stage of stimulation, and the seismicity rate remains high until the end of
481 stimulation, after which the seismicity rate decays rapidly. The stimulation and seismicity began a
482 day before the start of injection at Well 1, which is too distant (6 km away) to have an immediate
483 effect on the seismicity in Cluster 6. We therefore conclude that Cluster 6 was likely induced by
484 hydraulic fracturing. Similarly, Cluster 7 was also likely induced by hydraulic fracturing given the
485 strong spatial and temporal correlation between events in this cluster and stimulation at the nearest
486 production well 43153. For this cluster the seismicity rate remains high after stimulation has ceased.
487 The depth and orientation of events in Cluster 7 are not as accurate, given the greater distance away

488 from the seismic stations. Cluster 8 is spatially and temporally correlated with hydraulic fracturing
489 stimulation at nearby well 43258 in June 2010. The seismicity rate is initially high, then decreases
490 after the end of stimulation, but remains at a low level for over a month; however, there is no
491 seismicity in August 2010, following stimulation at another nearby well 43154. Cluster 8 may be the
492 same events, detected and located using a temporary seismic network by *Horton* [2012], that were
493 reported to lie on an east-west elongated trend near the Morrilton Fault east of injection well 3.

494 Cluster 9, which contains only 12 events, is located far from all production and injection wells,
495 and the magnitude-time plot does not show any temporal correlation with injection at Well 1 or 5, or
496 with stimulation at the nearest well 43154 located 2 km away. Therefore, we interpret these events
497 as natural background seismicity. The Enola swarms of 1982, with 30,000 earthquakes in 3 years
498 [*Chiu et al.*, 1984], and 2001, which had 2,500 earthquakes in 2 months with a M 4.4 as the largest
499 event [*Rabak et al.*, 2010], were natural earthquake sequences that occurred 2 km south of Box B3,
500 near 35.18°N, 92.2° W. The Enola swarms happened long before the start of hydraulic fracturing in
501 the Fayetteville Shale [*Horton*, 2012] or the start of wastewater injection in 2009 (Table S7).

502 The events in Cluster 10 could possibly be a result of hydraulic fracturing, but the quality of
503 our results is not sufficient to be definitive in this case. Event waveforms are noisy, leading to higher
504 location uncertainties. There are many production wells in the large area defining Cluster 10, which
505 are stimulated during over half the 3-month time period (Table S8): the magnitude-time plot for
506 Cluster 10 is mostly purple, so although the most of the high-seismicity time periods overlap with
507 stimulation, this temporal correlation is not informative.

508 Figure 14 closely examines seismicity located 4-8 kilometers northwest of the Guy-Greenbrier
509 Fault, within Clusters 11-13 (blue boxes) in Boxes 4 and 5 (Figure 1), and nearby stimulated
510 production wells. Magnitude-time plots once again highlight temporal correlations between well
511 activity and events in these clusters. Clusters 11 and 12 are just outside our seismic network, so
512 their depth estimates are probably reliable. In contrast, Cluster 13 is much farther away from the
513 network, so depths for these events are unreliable, and the event waveforms at WHAR are noisy.
514 The timing of events in Cluster 11, located directly on and oriented almost orthogonal to the well
515 path of the nearest production well 43439, overlaps closely with the duration of stimulation at well
516 43439, with a rapid decay of seismicity after stimulation ends, so Cluster 11 was likely induced by
517 hydraulic fracturing. Cluster 12, with only 14 events, is located about 1 km away from production
518 well 43433, but the temporal correlation with stimulation at this well is weak, since there is a long
519 delay between the end of stimulation and the seismicity. It is possible that these events, with a depth

of about 4 km, were triggered by pore pressure diffusion from injection at the nearest disposal Well 1 with a long time delay; however, we have no clear evidence to suggest that Cluster 12 events are not natural background seismicity. Cluster 13 was possibly induced by stimulation at nearby production wells 43254, 43255, and 43256 in late May and early June of 2010, after which the seismicity rate is very high. After the end of stimulation in early June, seismicity in Cluster 13 lingers at a low level during the entire 3-month study period, without being affected much by stimulation at wells 43252 and 43253 in July 2010. Many of the events in Cluster 13 were in the ANSS catalog (Figure S1).

Figure 15 shows magnitude-time plots for seismicity in Clusters 14-16, in various locations several kilometers away from the Guy-Greenbrier Fault (blue boxes labeled C14, C15, C16 in Figure 1). As these events are far from the seismic network, we detected very few events in these clusters, and their locations and depths are uncertain. Cluster 14 is most likely natural seismicity, since it is located far from any injection or production wells, and the events occur over the entire 3-month study period at a low background rate. Clusters 15 and 16 are spatially and temporally correlated with the duration of stimulation at the nearest production wells, 43244 and 43219 respectively, so they were likely induced by hydraulic fracturing.

3 Discussion

3.1 Microearthquakes induced by hydraulic fracturing are common during the Guy-Greenbrier sequence

Our analysis reveals that the initial stages of the Guy-Greenbrier earthquake sequence contain a complicated mixture of microseismicity with $M_L \leq 2.9$. The vast majority of these earthquakes are spatially and temporally related to hydraulic fracturing stimulation operations, which suggests that $M_L > 1$ seismicity induced by hydraulic fracturing is more common than widely appreciated. We identify about 3/4 (56/75) of ANSS catalog events as induced by hydraulic fracturing. Depending on the well, there is significant variation in the duration of seismicity after the end of stimulation. About 1/3 (17/53) of the production wells in this area stimulated during 2010-06-01 to 2010-09-01 are associated with seismicity (Table 2). We identify a smaller number of events, located on the Guy-Greenbrier Fault, which were likely induced by wastewater injection at Well 1 starting on 2010-07-07, and their migration southwest to greater depths anticipates the behavior of intense seismic activity to come in September and October 2010 [Ogwari *et al.*, 2016]. A small fraction of events that were uncorrelated with hydraulic fracturing or wastewater disposal may be natural background seismicity, which is known to occur in this area. Table 2 summarizes our preferred

551 interpretation for whether each cluster of earthquakes was natural, induced by injection, or induced
552 by hydraulic fracturing.

553 We suggest that much of the microseismicity later in the entire Guy-Greenbrier earthquake
554 sequence from September 2010 to October 2011, originally attributed to deep wastewater injection
555 [Horton, 2012; Huang and Beroza, 2015], may instead be a result of hydraulic fracturing stimulation.
556 Since the Guy-Greenbrier area has a history of natural seismicity from the Enola swarms in 1982
557 [Chiu *et al.*, 1984] and 2001 [Rabak *et al.*, 2010], one might consider the background seismicity
558 during June 2010, before the start of injection at Well 1, to be natural tectonic seismicity; however,
559 our study found that most of these "background" events were spatially and temporally associated with
560 hydraulic fracturing operations. We also found that many events during July and August 2010, after
561 the start of injection at Well 1, resulted from hydraulic fracturing rather than wastewater disposal,
562 with some of these events located very close to or on the Guy-Greenbrier Fault. Ogwari *et al.* [2016]
563 and Mousavi *et al.* [2017] reported a cluster of events west of the Guy-Greenbrier Fault that was likely
564 induced by hydraulic fracturing stimulation from 2010-09-29 to 2010-10-04; such events probably
565 also exist later in the sequence.

566 The combination of sensitive detection and precise location of microseismicity, and a detailed
567 public database of disposal wells and production wells with stimulation information, has allowed
568 us to separate events induced by hydraulic fracturing from events induced by wastewater injection
569 (Figure 12). The presence of these multiple influences on seismicity poses significant challenges for
570 seismic hazard mitigation, where different actions would be required for injection-induced seismicity
571 versus hydraulic fracturing-induced seismicity [Walters *et al.*, 2015]. All events during our study
572 period had $M_L \leq 2.9$, so they were too small to cause damage, but they do change the stresses
573 locally. Ogwari and Horton [2016] found that pore-pressure changes less than 0.06 MPa can initiate
574 seismicity on the critically stressed Guy-Greenbrier fault. We speculate that the presence of events,
575 such as those in Cluster 1, which are larger than expected for events caused by opening new fractures
576 [Warpinski *et al.*, 2012], could be a useful indicator that care should be taken with plans for nearby
577 large-scale wastewater injection.

578 **3.2 Benefits of high-sensitivity, high-resolution seismic monitoring**

579 We demonstrate that it is possible to extract detailed information on the location and timing of
580 microseismicity with a sparse 3-station seismic network recording continuously, with stations spaced
581 5-10 km apart, using high-resolution seismological techniques for event detection and location.

582 Methods that use waveform similarity to detect earthquakes in continuous seismic data, such as
583 template matching, the Repeating Signal Detector [Skoumal *et al.*, 2016], and FAST [Yoon *et al.*,
584 2015], can significantly improve the magnitude of completeness, allowing a statistical analysis of
585 seismicity rate changes over time and their relationship to fluid injection [Huang and Beroza, 2015],
586 and reveal unknown sources of low-magnitude seismicity, such as the clusters we found to be induced
587 by hydraulic fracturing. Many other studies have used template matching to identify seismicity
588 induced by hydraulic fracturing [Holland, 2013; Friberg *et al.*, 2014; Skoumal *et al.*, 2015a,b;
589 Schultz *et al.*, 2015a,b, 2016], as the magnitudes are often lower than for injection-induced seismicity
590 [Rutqvist *et al.*, 2013]. In addition to improved detection, we can obtain high-precision event locations
591 using double-difference relocation with cross-correlation derived travel times for similar pairs of
592 events [Waldhauser and Ellsworth, 2000], and subsequently obtain additional temporal resolution
593 with waveform cross-correlation. These types of detection, location, and correlation methods are
594 well suited for induced seismicity, where many events occur in close proximity as clusters, and thus
595 have similar waveforms when recorded at the same station. Limitations of our study include location
596 uncertainties due to the minimal 3-station network. We have poor depth constraints for events
597 outside the seismic network, and our absolute location uncertainty was 2 km even after improving
598 the velocity model with the quarry data. Nevertheless, the fortunate combination of a 3-station,
599 3-component continuous seismic network located near the seismicity and a high-quality public well
600 database with detailed records of injection and hydraulic fracturing stimulation allowed us to discern
601 the relationship between microseismicity, wastewater disposal, and hydraulic fracturing in this area.

602 In regions where seismic networks are sparse, our study suggests a cost-effective strategy for
603 seismic monitoring. A large number of stations is always helpful, but waveform-based detection
604 and location methods are essential for making the most out of a limited data set. It is preferable
605 for seismic stations to start recording continuously before the beginning of injection or stimulation
606 operations so that background seismicity can be measured. For example, we can envision running
607 single-station FAST at each station in a widely spaced permanent network to identify the existing
608 background rate of low-magnitude events. If the seismicity rate or the maximum magnitude of an
609 earthquake exceeds an acceptable threshold, or otherwise seems anomalous, a temporary network
610 with additional stations could be deployed to enable more detailed characterization of the earthquakes,
611 shifting limited resources where they are needed the most. Early awareness of changes in seismicity
612 can inform timely and informed decision making for operators and regulators about whether to
613 continue or alter injection and hydraulic fracturing activities, possibly as implemented in traffic light
614 systems for seismic risk management [Walters *et al.*, 2015].

4 Conclusions

In Guy-Greenbrier, Arkansas, an area of unconventional natural gas production in the Fayetteville Shale, wastewater injection beginning in July 2010 was widely suspected to have induced a year-long earthquake sequence that culminated in a M_w 4.7 earthquake [Horton, 2012; Huang and Beroza, 2015; Ogwari *et al.*, 2016]. We characterized seismicity at a very fine scale during the 3-month time period 2010-06-01 to 2010-09-01, which includes background seismicity, initiation of the Guy-Greenbrier earthquake sequence, and the early seismic response to wastewater injection, with $M_L \leq 2.9$ for all events. We used sensitive event detection methods: FAST [Yoon *et al.*, 2015], and template matching [Huang and Beroza, 2015], to detect 14,604 similar-waveform low-magnitude earthquakes in continuous seismic data at a single station. We followed this with precise relative double-difference location of nearby earthquakes [Waldhauser and Ellsworth, 2000] at three stations with an improved quarry-blast constrained velocity model, then harnessed waveform similarity to refine the temporal resolution of located event clusters. Most events during these 3 months were spatially and temporally correlated with hydraulic fracturing stimulation operations at a small number of nearby production wells, while we attribute a smaller number of events, located on and starting to outline the yet-to-be-discovered Guy-Greenbrier Fault, to wastewater injection at Well 1 starting in July 2010. Many stimulated production wells have no nearby detected seismicity. Although this area has hosted swarms of natural seismicity in the past [Chiu *et al.*, 1984; Rabak *et al.*, 2010], we infer that only a small fraction of events during these 3 months are natural in origin. The simultaneous presence of seismicity induced by both hydraulic fracturing and wastewater injection, which we speculate is also true later in the earthquake sequence, presents a challenge for seismic hazard mitigation and operational decision-making with traffic light systems [Walters *et al.*, 2015]. We demonstrate that given continuous seismic data and a detailed public well database with injection and stimulation information, it is possible to obtain high-resolution seismological observations even with a sparse 3-station network. We advocate continuous seismic monitoring for anomalous earthquake activity before starting injection or hydraulic fracturing.

Acknowledgments

The facilities of IRIS Data Services, and specifically the IRIS Data Management Center, were used for access to continuous seismic data used in this study (seismic networks AG and 7F). IRIS Data Services are funded through the Seismological Facilities for the Advancement of Geoscience and EarthScope (SAGE) Proposal of the National Science Foundation under Cooperative Agreement EAR-1261681. We obtained injection and production well data from the Arkansas Oil and Gas Commission Database

[AOGC, 2017a,b]. ANSS Comprehensive Earthquake Catalog (ComCat) data was downloaded from the U.S. Geological Survey website: <https://earthquake.usgs.gov/data/comcat/>. We ran FAST on high-performance computing clusters provided by the Stanford Center for Computational Earth and Environmental Science (CEES). We used Seismic Analysis Code (SAC) [Helffrich *et al.*, 2013] to manually pick P and S arrivals, ObsPy (with NumPy and Matplotlib) for seismological data processing and visualization [Beyreuther *et al.*, 2010], and Generic Mapping Tools (GMT) to generate maps [Wessel *et al.*, 2013]. Paul Ogwari showed us how to access stimulation data for Arkansas production wells [AOGC, 2017b] and shared valuable insights on the Guy-Greenbrier sequence. Mostafa Mousavi provided a detailed, thorough review of the initial manuscript. We thank Paul Friberg and Paul Ogwari for helpful reviews of the submitted manuscript. This paper also benefited from discussions with Mark Zoback, Rob Skoumal, Rongmao Zhou and Diane Frazier from BHP Billiton, and industrial affiliate members in the Stanford Center for Induced and Triggered Seismicity (SCITS). We thank Karianne Bergen for assistance with hierarchical clustering and Martin Schoenball for hypoDD help. C.Y. was funded by a Chevron Stanford Graduate Fellowship and by National Science Foundation grant EAR-1551462. The authors acknowledge financial support from SCITS.

References

- Arkansas Oil and Gas Commission (AOGC) (2017a). *Arkansas Well Data Search*, <http://www.aogc.state.ar.us/welldata/wells/default.aspx> (last accessed March 2017).
- Arkansas Oil and Gas Commission (AOGC) (2017b). *Arkansas DocuWare Document Imaging Wells File Cabinet*, <http://aogc2.state.ar.us:8080/DocuWare/PlatformRO/WebClient?orgId=1> (last accessed March 2017).
- Atkinson, G. M., Eaton, D. W., Ghofrani, H., Walker, D., Cheadle, B., Schultz, R., Shcherbakov, R., Tiampo, K., Gu, J., Harrington, R. M., Liu, Y., van der Baan, M., and Kao, H. (2016). Hydraulic Fracturing and Seismicity in the Western Canada Sedimentary Basin. *Seismol. Res. Lett.* 87, 3, doi:10.1785/0220150263.
- Bao, X. and Eaton, D. W. (2016). Fault activation by hydraulic fracturing in western Canada. *Science*, doi:10.1126/science.aag2583.
- Beyreuther, M., Barsch, R., Kischer, L., Megies, T., Behr, Y., and Wassermann, J. (2010). ObsPy: A Python toolbox for seismology. *Seismol. Res. Lett.* 81, 3, 530–533, doi:10.1785/gssrl.81.3.530.
- Bisrat, S., DeShon, H. R., and Rowe, C. (2012). Microseismic Swarm Activity in the New Madrid Seismic Zone. *Bull. Seismol. Soc. Am.* 102, 3, 1167–1178, doi:10.1785/0120100315.

- 678 Bormann, P. (Editor) (2012). Seismic Sources and Source Parameters, in *New Manual of*
679 *Seismological Observatory Practice (NMSOP-2)* (Chapter 3), IASPEI, GFZ German Research
680 Centre for Geosciences, Potsdam, ed. 2, <http://nmsop.gfz-potsdam.de> (last accessed July 2017),
681 doi:10.2312/GFZ.NMSOP-2.
- 682 British Columbia Oil and Gas Commission (BCOGC) (2012). *Investigation of Observed Seismicity*
683 *in the Horn River Basin*, <https://www.bco.gc.ca/node/8046/download> (last accessed June 2017).
- 684 British Columbia Oil and Gas Commission (BCOGC) (2014). *Investigation of Observed Seismicity*
685 *in the Montney Trend*, <https://www.bco.gc.ca/node/12291/download> (last accessed June 2017).
- 686 Cattaneo, M., Augliera, P., Spallarossa, D., and Lanza, V. (1999). A Waveform Similarity Approach
687 to Investigate Seismicity Patterns. *Natural Hazards* 19, 123–138.
- 688 Chiu, J. M., Johnston, A. C., Metzger, A. G., Haar, L., and Fletcher, J. (1984). Analysis of analog and
689 digital records of the 1982 Arkansas earthquake swarm. *Bull. Seismol. Soc. Am.* 74, 5, 1721–1742.
- 690 Clarke, H., Eisner, L., Styles, P., and Turner, P. (2014). Felt seismicity associated with shale
691 gas hydraulic fracturing: The first documented example in Europe. *Geophys. Res. Lett.* 41,
692 doi:10.1002/2014GL062047.
- 693 Davies, R., Foulger, G., Bindley, A., and Styles, P. (2013). Induced seismicity and
694 hydraulic fracturing for the recovery of hydrocarbons. *Mar. Pet. Geol.* 45, 171–185,
695 doi:10.1016/j.marpetgeo.2013.03.016.
- 696 Deichmann, N., and Garcia-Fernandez, M. (1992). Rupture geometry from high-precision relative
697 hypocentre locations of microearthquake clusters. *Geophys. J. Int.* 110, 501–517.
- 698 Ellsworth, W. L. (2013). Injection-induced earthquakes. *Science* 341, doi:10.1126/science.1225942.
- 699 Farahbod, A. M., Kao, H., Cassidy, J. F., and Walker, D. (2015). How did hydraulic-fracturing
700 operations in the Horn River Basin change seismicity patterns in northeastern British Columbia,
701 Canada? *The Leading Edge* 34, 658–663, doi:10.1190/tle34060658.1.
- 702 Fischer, T., and Guest, A. (2011). Shear and tensile earthquakes caused by fluid injection. *Geophys.*
703 *Res. Lett.* 38, L05307, doi:10.1029/2010GL045447.
- 704 Friberg, P. A., Besana-Ostman, G. M., and Dricker, I. (2014). Characterization of an earthquake
705 sequence triggered by hydraulic fracturing in Harrison County, Ohio. *Seismol. Res. Lett.* 85, 6,
706 1–13, doi:10.1785/0220140127.
- 707 Green, D. N., and Neuberg, J. (2006). Waveform classification of volcanic low-frequency earthquake
708 swarms and its implication at Soufriere Hills Volcano, Montserrat. *J. Volcanol. Geotherm. Res.*
709 153, 51–63, doi:10.1016/j.jvolgeores.2005.08.003.

- 710 Harris, D. (2006). Subspace detectors: Theory, *Lawrence Livermore Natl. Lab. Rep.*
711 *UCRL-TR-222758*, Lawrence Livermore National Laboratory, Livermore, California.
- 712 Harris, D. B. and Dodge, D. A. (2011). An Autonomous System for Grouping Events in a Developing
713 Aftershock Sequence. *Bull. Seismol. Soc. Am.* 101, 2, 763–774, doi:10.1785/0120100103.
- 714 Havskov, J., and Ottemoller, L. (2010). Location, in *Routine Data Processing*
715 *in Earthquake Seismology* (Chapter 5), Springer, New York, ed. 1, 101–150,
716 <https://link.springer.com/book/10.1007%2F978-90-481-8697-6>.
- 717 Healy, J. H., Rubey, W. W., Griggs, D. T., and Raleigh, C. B. (1968). The Denver earthquakes.
718 *Science* 161, 3848, 1301–1310.
- 719 Helffrich, G., Wookey, J., and Bastow, I. (2013). *The Seismic Analysis Code: A Primer and User's*
720 *Guide*, Cambridge University Press, United Kingdom, ed. 1.
- 721 Holland, A. A. (2013). Earthquakes Triggered by Hydraulic Fracturing in South-Central Oklahoma.
722 *Bull. Seismol. Soc. Am.* 103, 3, 1784–1792, doi:10.1785/0120120109.
- 723 Horton, S., (2012). Disposal of Hydrofracking Waste Fluid by Injection into Subsurface Aquifers
724 Triggers Earthquake Swarm in Central Arkansas with Potential for Damaging Earthquake. *Seismol.*
725 *Res. Lett.* 83, 2, 250–260, doi:10.1785/gssrl.83.2.250.
- 726 Huang, Y., Beroza, G. C., and Ellsworth, W. L. (2016). Stress drop estimates of potentially
727 induced earthquakes in the Guy-Greenbrier sequence. *J. Geophys. Res. Solid Earth* 121, 1–11,
728 doi:10.1002/2015GL065170.
- 729 Huang, Y., and Beroza, G. C. (2015). Temporal variation in the magnitude-frequency
730 distribution during the Guy-Greenbrier earthquake sequence. *Geophys. Res. Lett.* 42, 6639–6646,
731 doi:10.1002/2016JB013067.
- 732 Hurd, O., and Zoback, M. D. (2012). Intraplate earthquakes, regional stress and fault mechanics
733 in the Central and Eastern U.S. and Southeastern Canada. *Tectonophysics* 581, 182–192,
734 doi:10.1016/j.tecto.2012.04.002.
- 735 Kafka, A. L. (1990). *R_g* as a Depth Discriminant for Earthquakes and Explosions: A Case Study in
736 New England. *Bull. Seismol. Soc. Am.* 80, 2, 373–394.
- 737 Kissling, E., Ellsworth, W. L., Eberhart-Phillips, D., and Kradolfer, U. (1994). Initial reference
738 models in local earthquake tomography. *J. Geophys. Res.* 99, 19,635–19,646.
- 739 Leskovec, J., Rajaraman, A., and Ullman, J. D. (2014). Clustering, in *Mining of Massive Datasets*
740 (Chapter 7), Cambridge University Press, New York, ed. 2, 73–130, <http://www.mmms.org>.
- 741 Maeda, N. (1985). A method for reading and checking phase times in auto- processing system of
742 seismic wave data. *Zisin=Jishin* 38, 365–379.

- 743 Massa, M., Eva, E., Spallarossa, D., and Eva, C. (2006). Detection of earthquake clusters on the basis
744 of waveform similarity: An application in the monferrato region (Piedmont, Italy). *J. Seismol.* 10,
745 1–22, doi:10.1007/s10950-006-2840-4.
- 746 Maxwell, S. C., Jones, M. B., Parker, R. L., Leaney, W. S., Mack, M., Dorval, D., D'Amico,
747 D., Logel, J., Anderson, E., and Hammermaster, K. (2010). Fault activation during hydraulic
748 fracturing. *AAPG Search Discov* 90172, doi:10.1190/1.3255145.
- 749 Maxwell, S. (2013). Unintentional Seismicity Induced by Hydraulic Fracturing. *CSEG Rec.* 38,
750 40–49.
- 751 Mousavi, S. M., Ogwari, P. O., Horton, S. P., and Langston, C. A. (2017). Spatio-temporal evolution of
752 frequency-magnitude distribution and seismogenic index during initiation of induced seismicity at
753 Guy-Greenbrier, Arkansas. *Phys. Earth Planet. Inter.* 267, 53–66, doi:10.1016/j.pepi.2017.04.005.
- 754 Ogwari, P. O., Horton, S. P., and Ausbrooks, S. (2016). Characteristics of Induced/ Triggered
755 Earthquakes during the Startup Phase of the Guy-Greenbrier Earthquake Sequence in
756 North-Central Arkansas. *Seismol. Res. Lett.* 87, 3, doi:10.1785/0220150252.
- 757 Ogwari, P. O., and Horton, S. P. (2016). Numerical model of pore-pressure diffusion associated with
758 the initiation of the 2010-2011 Guy-Greenbrier, Arkansas earthquakes. *Geofluids* 16, 954–970,
759 doi:10.1111/gfl.12198.
- 760 Petersen, T. (2007). Swarms of repeating long-period earthquakes at Shishaldin Volcano, Alaska,
761 2001-2004. *J. Volcanol. Geotherm. Res.* 166, 177–192, doi:10.1016/j.jvolgeores.2007.07.014.
- 762 Prejean, S. G., and Ellsworth, W. L. (2001). Observations of Earthquake Source Parameters at 2 km
763 Depth in the Long Valley Caldera, Eastern California. *Bull. Seismol. Soc. Am.* 91, 2, 165–177.
- 764 Rabak, I., Langston, C., Bodin, P., Horton, S., Withers, M., and Powell, C. (2010).
765 The Enola, Arkansas, Intraplate Swarm of 2001. *Seismol. Res. Lett.* 81, 3, 549–559,
766 doi:10.1785/gssrl.81.3.549.
- 767 Raleigh, C. B., Healy, J. H., and Bredehoeft, J. D. (1976). An experiment in earthquake control at
768 Rangely, Colorado. *Science* 191, 4233, 1230–1237, doi:10.1126/science.191.4233.1230.
- 769 Rowe, C. A., Thurber, C. H., and White, R. A. (2004). Dome growth behavior at Soufriere Hills
770 Volcano, Montserrat, revealed by relocation of volcanic event swarms, 1995-1996. *J. Volcanol.*
771 *Geotherm. Res.* 134, 199–221, doi:10.1016/j.jvolgeores.2004.01.008.
- 772 Rubinstein, J. L. and Mahani, A. B. (2015). Myths and Facts on Wastewater Injection,
773 Hydraulic Fracturing, Enhanced Oil Recovery, and Induced Seismicity. *Seismol. Res. Lett.* 86,
774 doi:10.1785/0220150067.

- 775 Rutqvist, J., Rinaldi, A. P., Cappa, F., and Moridis, G. J. (2013). Modeling of fault reactivation
776 and induced seismicity during hydraulic fracturing of shale-gas reservoirs. *J. Pet. Sci. Eng.* 107,
777 31–44, doi:10.1016/j.petrol.2013.04.023.
- 778 Schaff, D. P., Bokelmann, G. H. R., Ellsworth, W. L., Zankerka, E., Waldhauser, F., and Beroza, G. C.
779 (2004). Optimizing Correlation Techniques for Improved Earthquake Location. *Bull. Seismol. Soc.*
780 *Am.* 94, 2, 705–721.
- 781 Schultz, R., Stern, V., Novakovic, M., Atkinson, G., and Gu, Y. J. (2015a). Hydraulic fracturing and
782 the Crooked Lake Sequences: Insights gleaned from regional seismic networks. *Geophys. Res.*
783 *Lett.* 42, 2750–2758, doi:10.1002/2015GL063455.
- 784 Schultz, R., Mei, S., Pana, D., Gu, Y. J., Kim, A., and Eaton, D. (2015b). The Cardston Earthquake
785 Swarm and Hydraulic Fracturing of the Exshaw Formation (Alberta Bakken Play). *Bull. Seismol.*
786 *Soc. Am.* 105, 6, doi:10.1785/0120150131.
- 787 Schultz, R., Wang, R., Gu, Y. J., Haug, K., and Atkinson, G. (2016). A seismological overview of the
788 induced earthquakes in the Duvernay play near Fox Creek, Alberta. *J. Geophys. Res. Solid Earth*
789 122, doi:10.1002/2016JB013570.
- 790 Shapiro, S. A., Rothert, E., Rath, V., and Rindschwentner, J. (2002). Characterization of fluid
791 transport properties of reservoirs using induced microseismicity. *Geophysics* 67, 1, 212–220,
792 doi:10.1190/1.1451597.
- 793 Shapiro, S. A., and Dinske, C. (2009). Fluid-induced seismicity: Pressure diffusion and hydraulic
794 fracturing. *Geophysical Prospecting* 57, 301–310, doi:10.1111/j.1365-2478.2008.00770.x.
- 795 Sileny, J., Hill, D. P., Eisner, L., and Cornet, F. H. (2009). Non–double-couple mechanisms
796 of microearthquakes induced by hydraulic fracturing. *J. Geophys. Res.* 114, B08307,
797 doi:10.1029/2008JB005987.
- 798 Skoumal, R. J., Brudzinski, M. R., and Currie, B. S. (2015a). Earthquakes Induced by
799 Hydraulic Fracturing in Poland Township, Ohio. *Bull. Seismol. Soc. Am.* 105, 1, 189–197,
800 doi:10.1785/0120140168.
- 801 Skoumal, R. J., Brudzinski, M. R., and Currie, B. S. (2015b). Distinguishing induced seismicity
802 from natural seismicity in Ohio: Demonstrating the utility of waveform template matching. *J.*
803 *Geophys. Res. Solid Earth* 120, 6284–6296, doi:10.1002/2015JB012265.
- 804 Skoumal, R. J., Brudzinski, M. R., and Currie, B. S. (2016). An efficient repeating signal
805 detector to investigate earthquake swarms. *J. Geophys. Res. Solid Earth* 121, 5880–5897,
806 doi:10.1002/2016JB012981.

- 807 Thelen, W. A., Allstadt, K., De Angelis, S., Malone, S. D., Moran, S. C., and Vidale, J. (2013).
808 Shallow repeating seismic events under an alpine glacier at Mount Rainier, Washington, USA. *J.*
809 *Glaciol.* 59, 214, 345–356, doi:10.3189/2013JoG12J111.
- 810 Vavrycuk, V. (2011). Tensile earthquakes: Theory, modeling, and inversion. *J. Geophys. Res.* 116,
811 B12320, doi:10.1029/2011JB008770.
- 812 Vermylen, J. P., and Zoback, M. D. (2011). Hydraulic fracturing, microseismic magnitudes, and stress
813 evolution in the Barnett Shale, Texas, USA. Paper SPE-140507-MS presented at SPE Hydraulic
814 Fracturing Conference. Society of Petroleum Engineers, The Woodlands, Tex.
- 815 Waldhauser, F., and Ellsworth, W. L. (2000). A Double-Difference Earthquake Location Algorithm:
816 Method and Application to the Northern Hayward Fault, California. *Bull. Seismol. Soc. Am.* 90,
817 6, 1353–1368.
- 818 Walters, R. J., Zoback, M. D., Baker, J. W., and Beroza, G. C. (2015). Characterizing and
819 Responding to Seismic Risk Associated with Earthquakes Potentially Triggered by Fluid Disposal
820 and Hydraulic Fracturing. *Seismol. Res. Lett.* 86, 4, doi:10.1785/0220150048.
- 821 Wang, R., Gu, Y. J., Schultz, R., Kim, A., and Atkinson, G. (2016). Source analysis of a
822 potential hydraulic-fracturing-induced earthquake near Fox Creek, Alberta. *Geophys. Res. Lett.*
823 43, 564–573, doi:10.1002/2015GL066917.
- 824 Warpinski, N. R., Du, J., and Zimmer, U. (2012). Measurements of Hydraulic-Fracture-Induced
825 Seismicity in Gas Shales. *PE Hydraul. Fract. Technol. Conf., SPE 151597*, The Woodlands,
826 Texas, 6-8 February 2012, doi:10.2118/151597-PA.
- 827 Wessel, P., Smith, W. H. F., Scharroo, R., Luis, J. F., and Wobbe, F. (2013). Generic Mapping Tools:
828 Improved version released. *Eos Trans. AGU* 94, 409–410, doi:10.1002/2013EO450001.
- 829 Yoon, C. E., O'Reilly, O., Bergen, K. J., and Beroza, G. C. (2015). Earthquake
830 detection through computationally efficient similarity search. *Science Advances* 1, e1501057,
831 doi:10.1126/sciadv.1501057.

832 **Table 1.** New 1D velocity model, constrained by quarry blast location, used to locate all earthquakes in this
833 study.

Depth (km)	P wave (km/s)	S wave (km/s)	V_p/V_s
0.0	4.06	2.46	1.650
1.22	5.57	3.22	1.730
2.89	6.12	3.27	1.872
6.23	6.23	3.58	1.740
13.0	6.24	3.71	1.682

834 **Table 2.** Summary of 16 seismicity clusters from 2010-06-01 to 2010-09-01, names of wells associated
835 with each cluster, and our preferred interpretation of whether they are natural, induced by hydraulic fracturing
836 stimulation, or induced by wastewater injection at Well 1.

Cluster Number	Interpretation	Associated Well Names
1	Hydraulic fracturing	42146, 42389, 42262, 43344, 43343
2	Hydraulic fracturing	42069, 43375, 43376
3	Wastewater injection	Injection Well 1
4	Wastewater injection	Injection Well 1
5	Wastewater injection	Injection Well 1
6	Hydraulic fracturing	43043
7	Hydraulic fracturing	43153
8	Hydraulic fracturing	43258
9	Natural	–
10	Hydraulic fracturing	Several wells, but not definitive
11	Hydraulic fracturing	43439
12	Natural	–
13	Hydraulic fracturing	43254, 43255, 43256
14	Natural	–
15	Hydraulic fracturing	43244
16	Hydraulic fracturing	43219

837 **Figure 1.** Map of Guy-Greenbrier area in central Arkansas (red box, inset at lower left) with earthquake
838 locations, seismic stations, wastewater injection wells, and production wells with hydraulic fracturing stimulation
839 during the time period 2010-06-01 to 2010-09-01. Profile A-A' shows only seismicity located within 0.5 km
840 of the Guy-Greenbrier Fault. Profile B-B', perpendicular to the Guy-Greenbrier Fault, shows all seismicity:
841 circled events are located on the Guy-Greenbrier Fault, while other seismicity is off the Guy-Greenbrier Fault.
842 The profiles include locations of ANSS catalog events after this time period (small gray dots) to delineate the
843 location of the Guy-Greenbrier Fault. Later figures zoom in on areas enclosed in red boxes B1-B5 (B1 and
844 B2 in Figure 8, B3 in Figure 13, B4 and B5 in Figure 14). Blue boxes C14-C16 indicate isolated clusters of
845 seismicity discussed in Section 2.7. Fault traces are from *Horton* [2012].

846 **Figure 2.** Schematic illustration of combining FAST similarity matrix output from multiple components
 847 at a single station WHAR as sparse matrix addition. Each square represents a pair of fingerprints (which
 848 can be mapped back to waveforms) from two different times in the continuous data. Gray squares with high
 849 similarity indicate times when similar waveforms occur for each component. Black squares indicate times when
 850 waveforms are similar on all 3 components.

851 **Figure 3.** Comparison of earthquakes detected by FAST and template matching during the time period
 852 2010-06-01 to 2010-09-01. Both methods detect the same 12,368 events (blue). FAST detects an additional
 853 658 events that template matching did not find (cyan), while template matching detected 1,578 events that FAST
 854 fails to detect (magenta). We detect a total of 14,604 events using either FAST, template matching, or both
 855 methods.

856 **Figure 4.** (a) Three quarry blasts with similar waveforms recorded between 2010-06-01 and 2010-09-01. (b)
 857 Google Earth satellite imagery from before (2009-07-23) and after (2010-09-15) the 3 quarry blasts. We infer
 858 that the blasting occurred at the circled notch (red), which is present in the post-blast image but absent from the
 859 pre-blast image. This notch location is used as ground truth for the 3 quarry blasts, allowing us to refine the
 860 velocity model.

861 **Figure 5.** 1D velocity model comparison. We use the updated Central Arkansas 1D velocity model from
 862 Table 3 in *Ogwari et al.* [2016] (dashed) as a starting model, then calculate a refined velocity model constrained
 863 by the quarry blast location (solid). The refined model has slightly lower P and S wave velocities at shallow
 864 depth and is used to locate all earthquakes in this study.

865 **Figure 6.** Magnitude-frequency distribution of all 14,604 detected events (Figure 3): 1,740 located events
 866 (blue), 6,508 assigned events (black), 6,356 unassigned events (red). Although we were unable to locate
 867 the assigned events, we can categorize them as belonging to Clusters 1-16 through cross-correlation of event
 868 waveforms at station WHAR (Section 2.6). The predominantly low-magnitude unassigned events are the
 869 remaining detected events from Figure 3 that are too noisy to either locate or associate with existing clusters.
 870 The largest 3 events were not located because they occurred before 2010-06-11, when data was available only
 871 at station WHAR.

872 **Figure 7.** Representative stack waveform (top) and normalized waveforms aligned with cross-correlation
 873 (bottom) of all 3,192 earthquakes belonging to Cluster 1, recorded on each component of station WHAR (east:
 874 left; north: center; vertical: right). We located the 667 largest events (shaded orange) in Cluster 1. Although
 875 we were unable to locate the 2,525 lower-magnitude events due to a lack of high-quality picks at stations ARK1
 876 and ARK2, their waveforms at station WHAR are similar to the located event waveforms, so they can be used
 877 to improve the temporal resolution of events in Cluster 1.

878 **Figure 8.** Zoomed map view of seismicity in Clusters 1-5 (blue boxes), Boxes 1-2 (red boxes in Figure 1 -
879 see legend), and their spatial and temporal relationship to nearby stimulated production wells (small triangles
880 colored by depth, labeled by permit number from Table S8, listed for each cluster in last column of Table S5)
881 and wastewater injection wells (inverted triangles colored by depth). Earthquakes on the map are circles colored
882 by depth and sized by relative magnitude. These events are located on or near the labeled Guy-Greenbrier Fault,
883 with \sim N30°E strike [Horton, 2012; Ogwari *et al.*, 2016]. Thick black arrows indicate the \sim N60°E orientation
884 of maximum horizontal compressive stress in this region [Hurd and Zoback, 2012].

885 **Figure 9.** Time evolution of seismicity in Cluster 1, and hydraulic fracturing stimulation at the 5 nearest
886 production wells (labeled by permit number from Table S8), near north end of the Guy-Greenbrier Fault.
887 Earthquakes (circles sized by relative magnitude), as well as stimulated sections of the production wells during
888 each stage of hydraulic fracturing, are colored by time with Day 0 defined as 2010-07-16 00:00:00 UTC. (a)
889 Actual seismicity locations, which exhibit an offset from the well paths. (b) Seismicity locations shifted \sim 0.7
890 km southeast relative to the locations from (a), which makes it easier to see the spatial and temporal correlations
891 between seismicity and stimulation stages. We display these shifted locations in Figure 10 and Movie S1. The
892 shifted locations, which are within the 2 km absolute location uncertainty, agree with the back-azimuth derived
893 from P-wave polarization analysis at station ARK2 (Figure S5).

894 **Figure 10.** Time evolution of seismicity in Cluster 1, and hydraulic fracturing stimulation at the 5 nearest
895 production wells (labeled by permit number from Table S8), near north end of the Guy-Greenbrier Fault.
896 We display the shifted seismicity locations from Figure 9b. In (a)-(d), earthquakes (circles sized by relative
897 magnitude), as well as stimulated sections of the production wells during each stage of hydraulic fracturing, are
898 colored by time with Day 0 defined as 2010-07-16 00:00:00 UTC. This figure shows seismicity and stimulated
899 stages during different time intervals after the start of stimulation: (a) 0 days to 3 days 8 hours, with early
900 stimulations at wells 43343 and 43344; (b) 3 days 8 hours to 6 days 8 hours, with later stimulations at wells
901 43343 and 43344, and early stimulations at wells 42146 and 42389; (c) 6 days 8 hours to 10 days 6 hours,
902 with later stimulations at wells 42146 and 42389; (d) 10 days 6 hours to 16 days, with stimulations at well
903 42262. Movie S1 displays cumulative Cluster 1 seismicity and stages of stimulation for the entire 16-day time
904 period. (e) Time evolution of magnitudes for located (blue) and assigned (black) events during the 16 days
905 of stimulation, with labeled time intervals for (a)-(d). We plot the stimulation duration of all stages from a
906 particular production well in a different color.

907 **Figure 11.** (a) Map view of selected east-west oriented events (colored by depth, sized by relative magnitude)
 908 in Clusters 1, 2, 3C with first motions represented on composite focal mechanism. Cluster 1 events are shifted
 909 ~0.7 km southeast as in Figure 9b. Nearby stimulated production wells (small triangles colored by depth,
 910 labeled by permit number from Table S8) and wastewater injection wells (inverted triangle colored by depth) are
 911 shown. (b) Composite focal mechanism from first motion polarity (black "u": up, red "d": down) of selected
 912 events in Clusters 1, 2, 3C, on lower hemisphere projection. Black lines show nodal planes that best fit the first
 913 motion polarity data, assuming a double-couple source. Thick black arrows indicate the ~N60°E orientation of
 914 maximum horizontal compressive stress in this region [Hurd and Zoback, 2012].

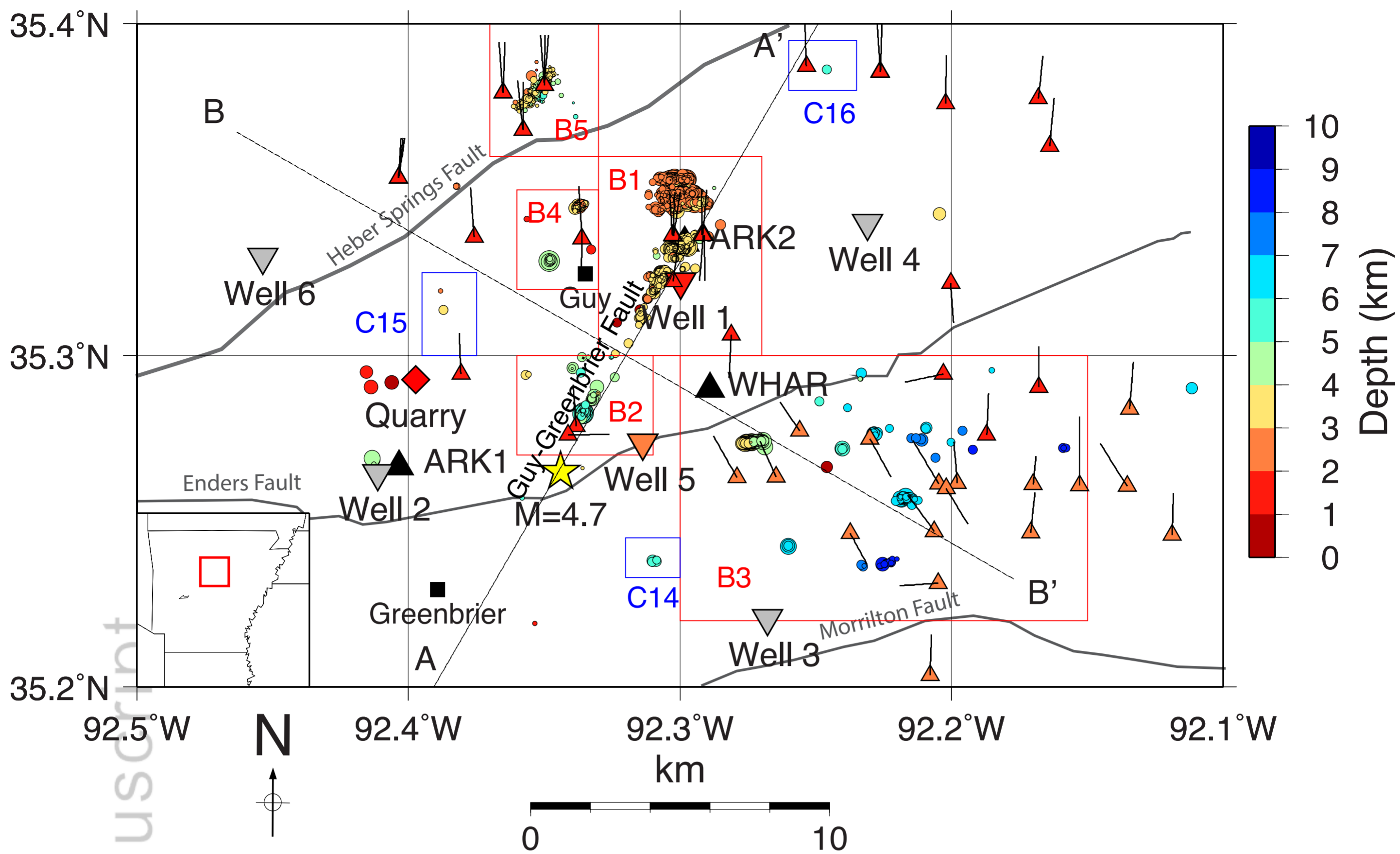
915 **Figure 12.** Summary of seismicity located within 0.5 km of the Guy-Greenbrier Fault, with wastewater
 916 injection Wells 1 and 5 (Table S7), along the southwest to northeast cross-section Profile A-A' (Figure 1).
 917 Earthquakes are circles colored by depth and sized by relative magnitude. Clusters 1 and 2 (blue boxes labeled
 918 as C1, C2) were likely induced by hydraulic fracturing stimulation. The remaining events belonging to Clusters
 919 3, 4, 5 were probably induced by wastewater injection at Well 1. (a) Depth of events as a function of along-strike
 920 distance. Later ANSS catalog event locations (small gray dots), from 2010-09-01 to 2011-10-31, delineate
 921 the depth extent of the Guy-Greenbrier Fault. Magenta section shows the depth of wastewater injection at
 922 Wells 1 and 5. Depths for the Fayetteville Shale, Boone Formation/Ozark Aquifer, and Precambrian basement
 923 were obtained from *Ogwari et al.* [2016]. (b) Time of events and wastewater injection (arrows) as a function
 924 of along-strike distance. We estimate a hydraulic diffusivity of $D \approx 1 \text{ m}^2/\text{s}$ for pore pressure diffusion from
 925 injection at Well 1.

926 **Figure 13.** Zoomed map view of seismicity in Clusters 6-10 (blue boxes), Box 3 (red box in Figure 1 -
 927 see legend), and their spatial and temporal relationship to nearby stimulated production wells (small triangles
 928 colored by depth, labeled by permit number from Table S8, listed for each cluster in last column of Table S5).
 929 Earthquakes on the map are circles colored by depth and sized by relative magnitude. These events are located
 930 off the main Guy-Greenbrier Fault, to the southeast.

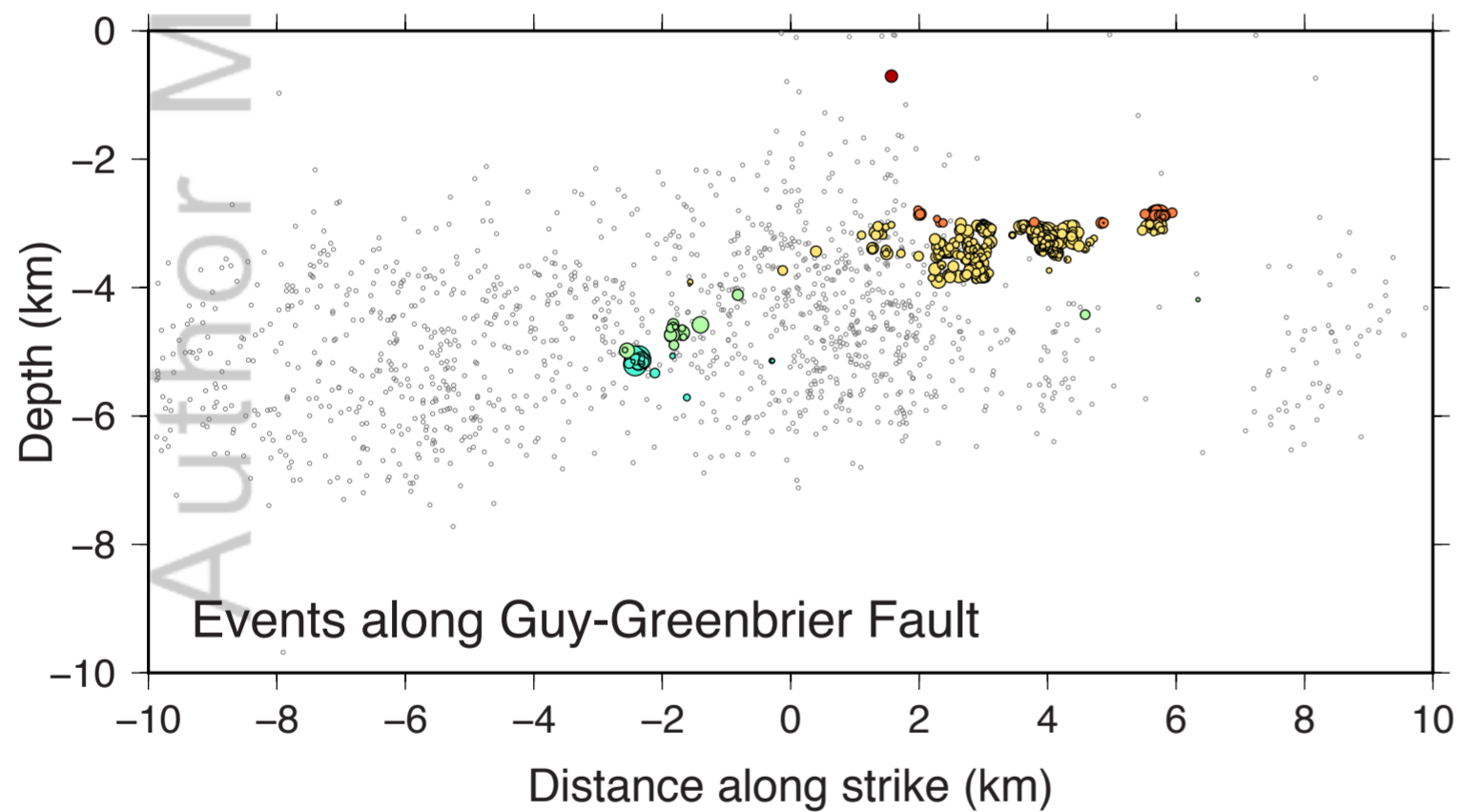
931 **Figure 14.** Zoomed map view of seismicity in Clusters 11-13 (blue boxes), Boxes 4-5 (red boxes in Figure 1
 932 - see legend), and their spatial and temporal relationship to nearby stimulated production wells (small triangles
 933 colored by depth, labeled by permit number from Table S8, listed for each cluster in last column of Table S5).
 934 Earthquakes on the map are circles colored by depth and sized by relative magnitude. These events are located
 935 off the main Guy-Greenbrier Fault, to the northwest.

936 **Figure 15.** Seismicity in Clusters 14-16 (locations in blue boxes, Figure 1), and their temporal relationship to
 937 nearby stimulated production wells (listed for each cluster in last column of Table S5) and wastewater injection
 938 wells. These events are in isolated clusters located off the main Guy-Greenbrier Fault.

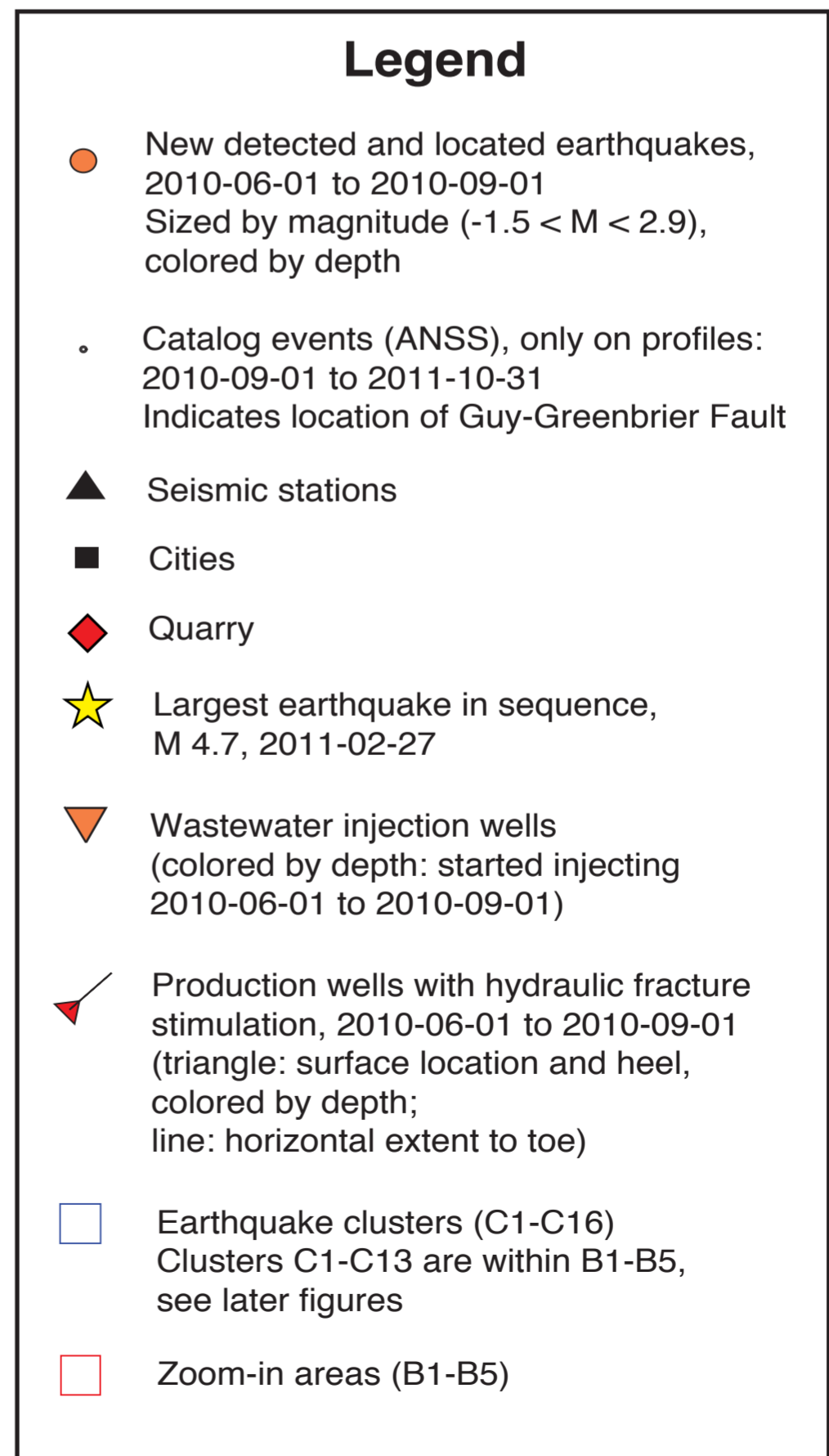
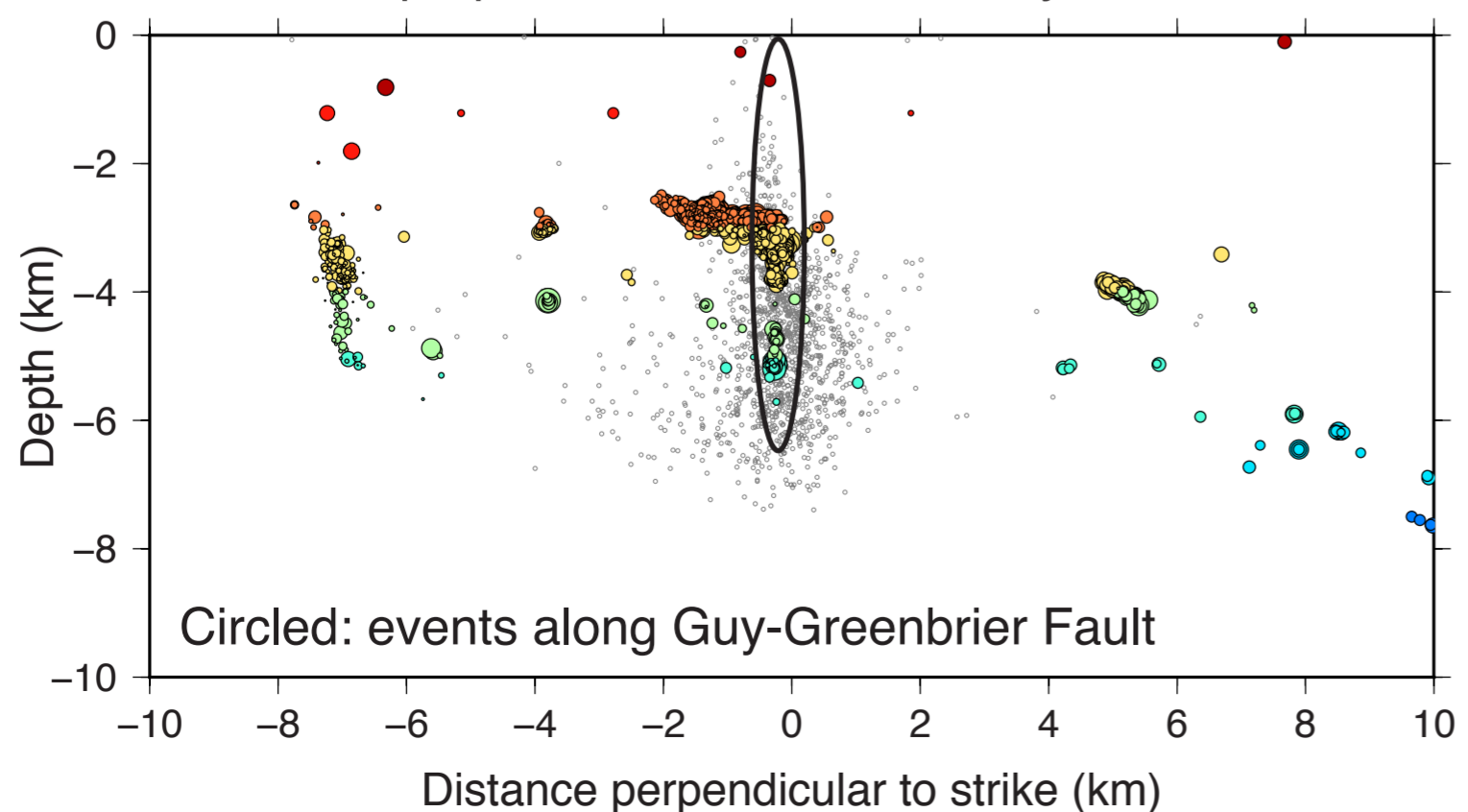
Author Manuscript



Profile A–A' along strike of Guy–Greenbrier Fault

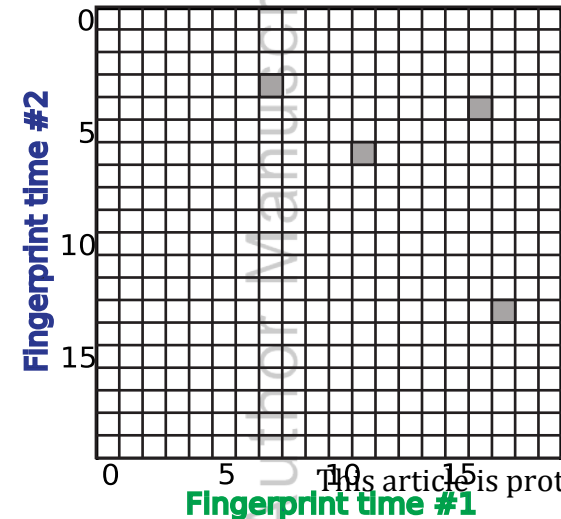


Profile B–B' perpendicular to strike of Guy–Greenbrier Fault



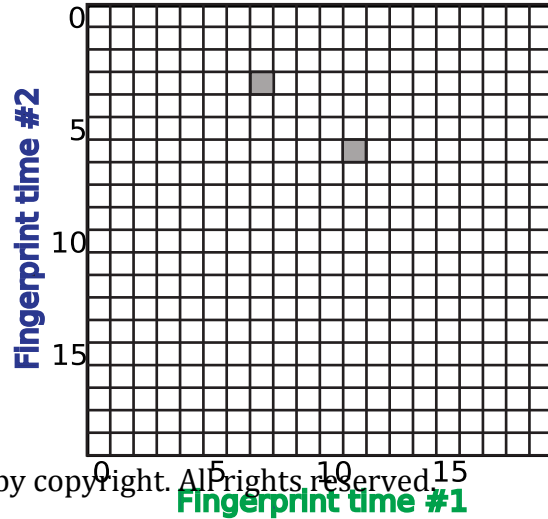
Author Manuscript

WHAR.HHE



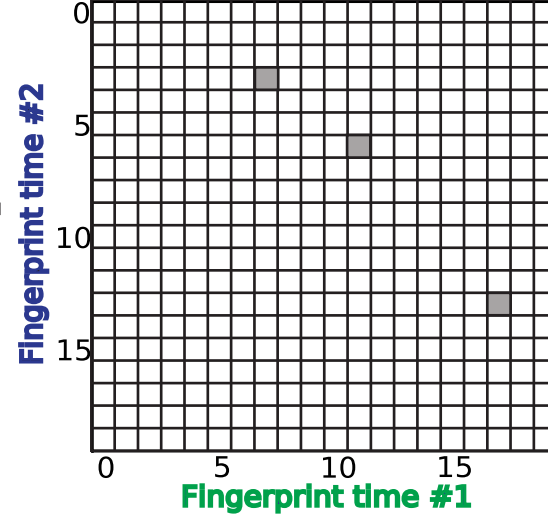
+

WHAR.HHN



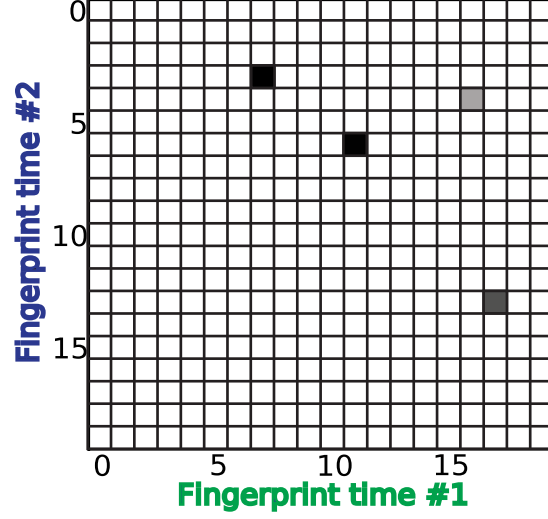
+

WHAR.HHZ



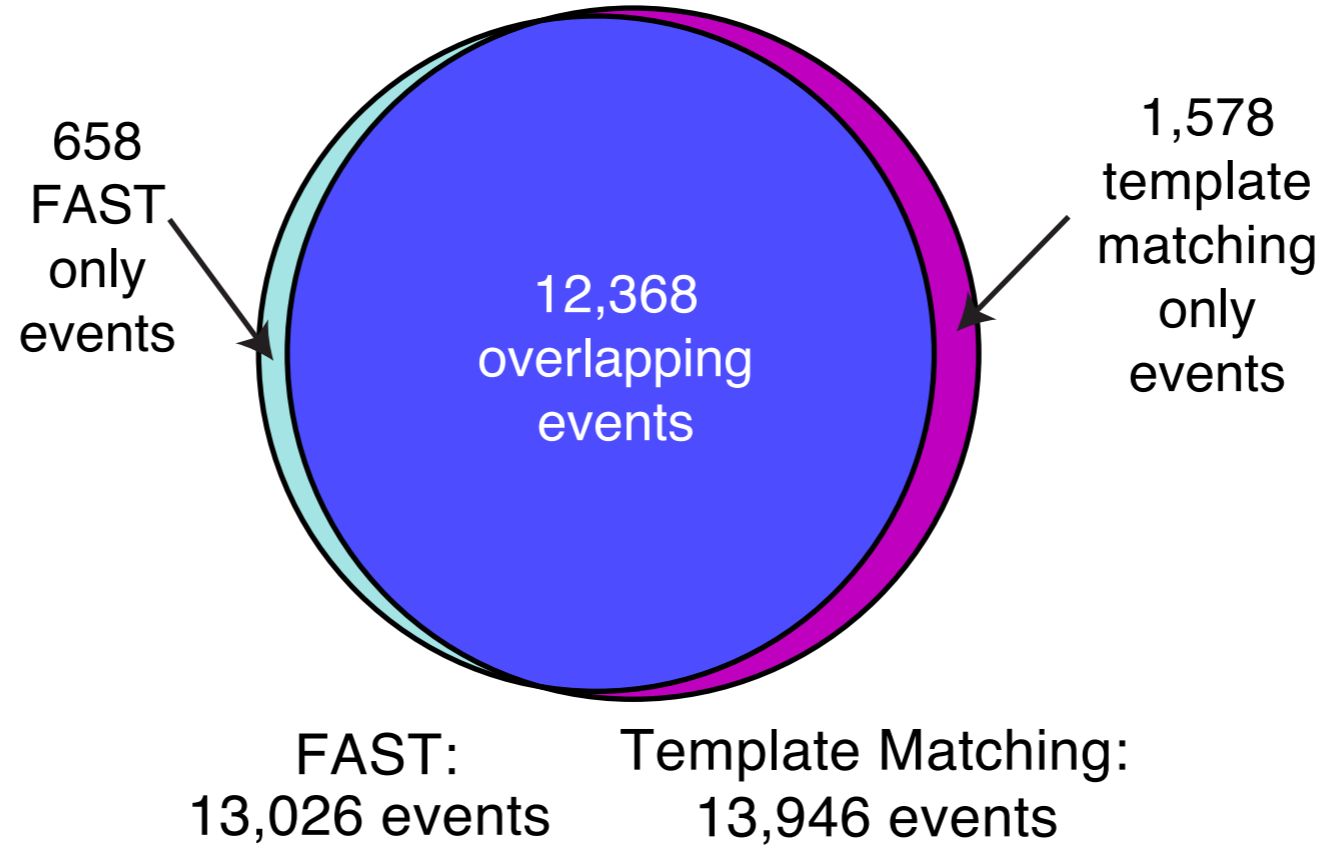
=

WHAR 3 Component

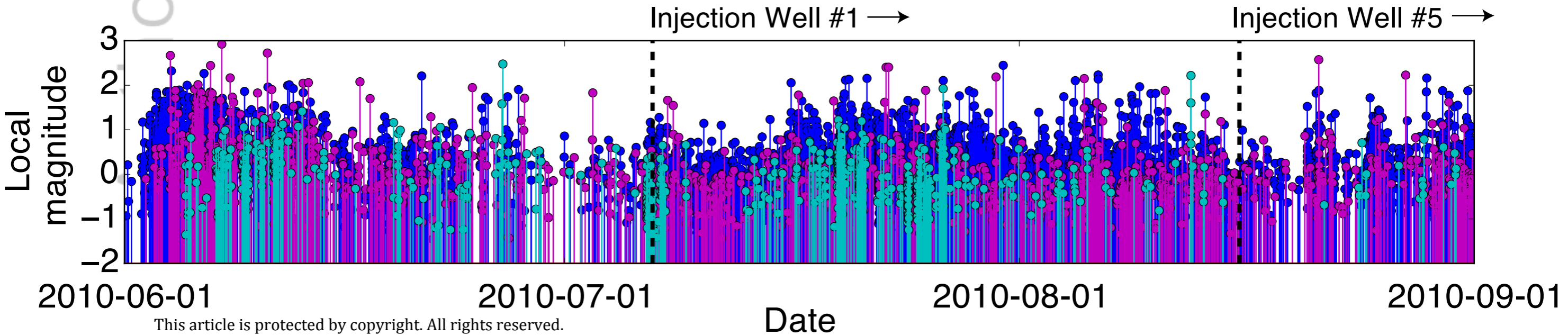


Author Manuscript

Total: 14,604 detected events



Single station earthquake detections, 2010-06-01 to 2010-09-01

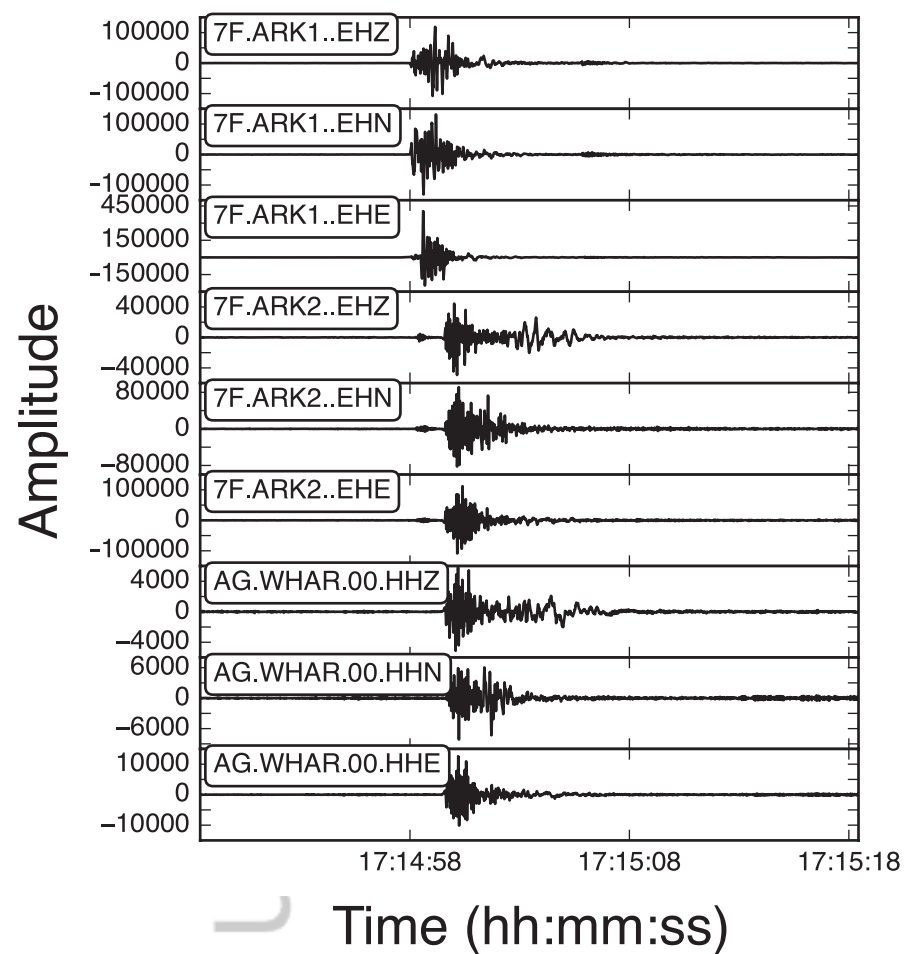


Author Manuscript

a)

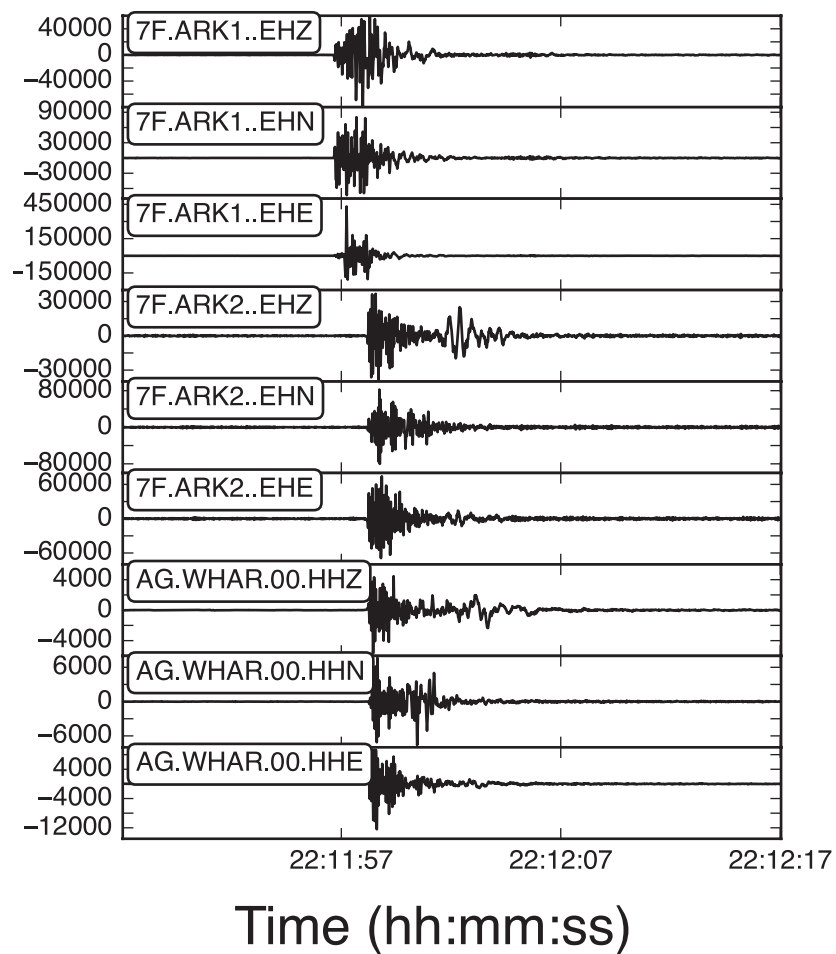
2010-06-24

2010-06-24T17:14:48.44 - 2010-06-24T17:15:18.44



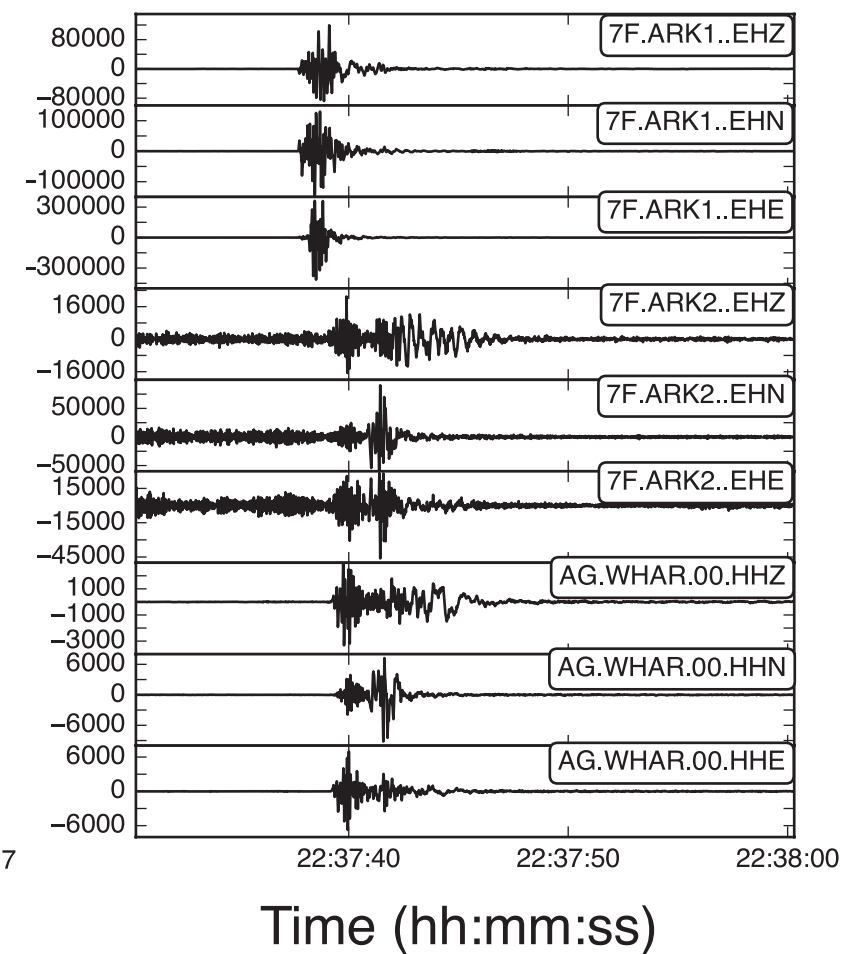
2010-07-02

2010-07-02T22:11:47.04 - 2010-07-02T22:12:17.04



2010-08-10

2010-08-10T22:37:30.3 - 2010-08-10T22:38:00.3

**b)**

Quarry, 2009-07-23

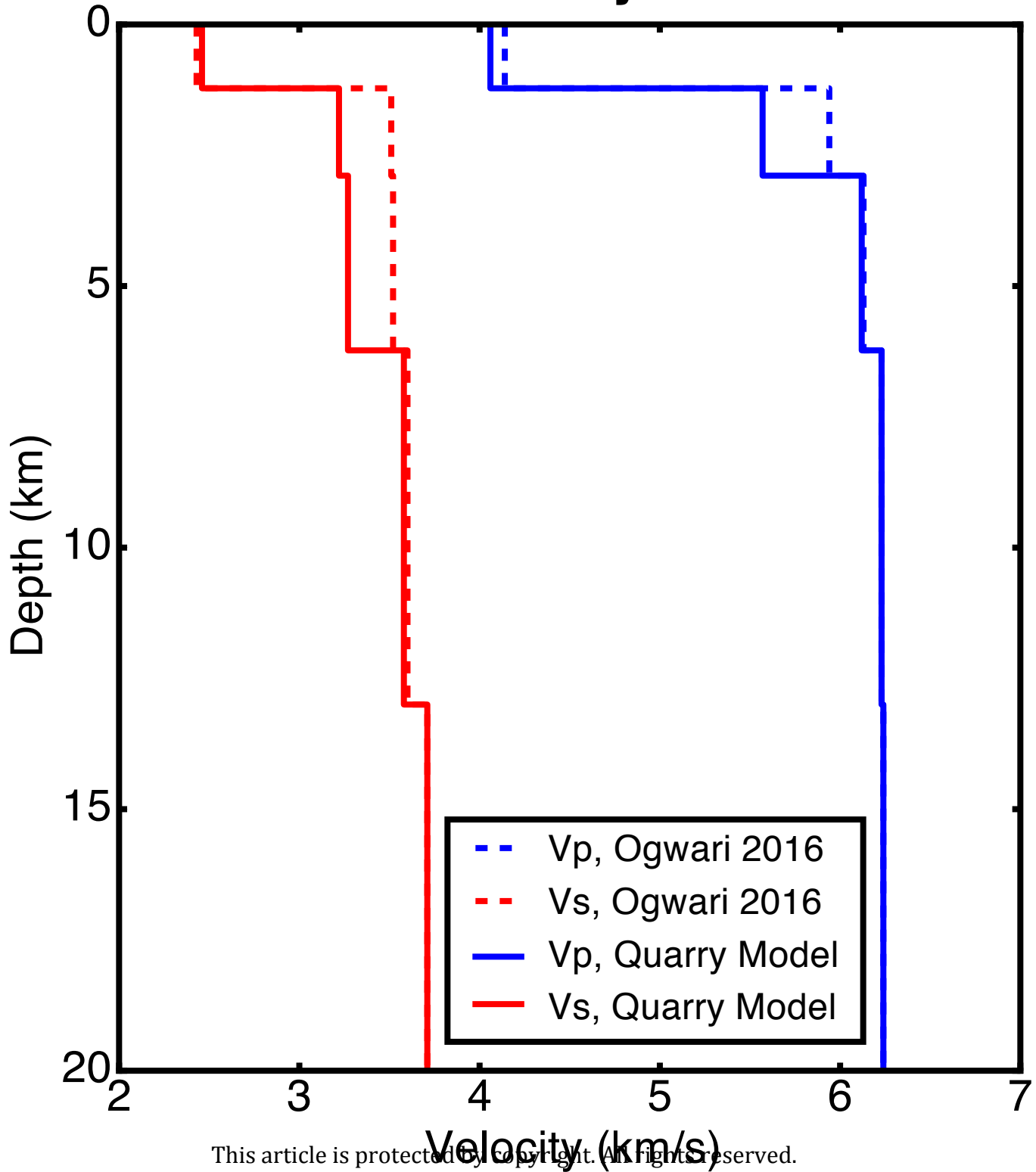


Quarry, 2010-09-15



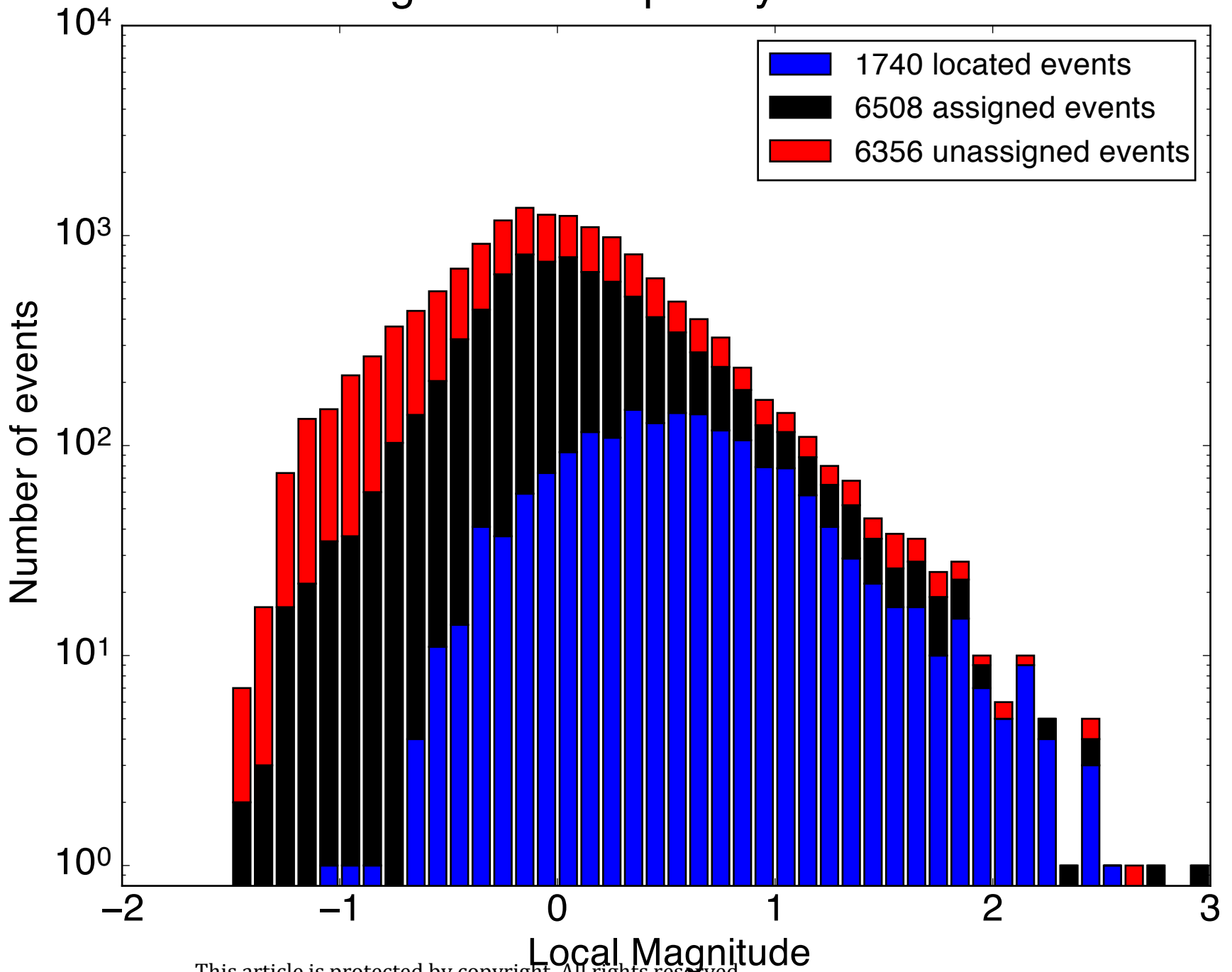
Author Manuscript

1D Velocity Model

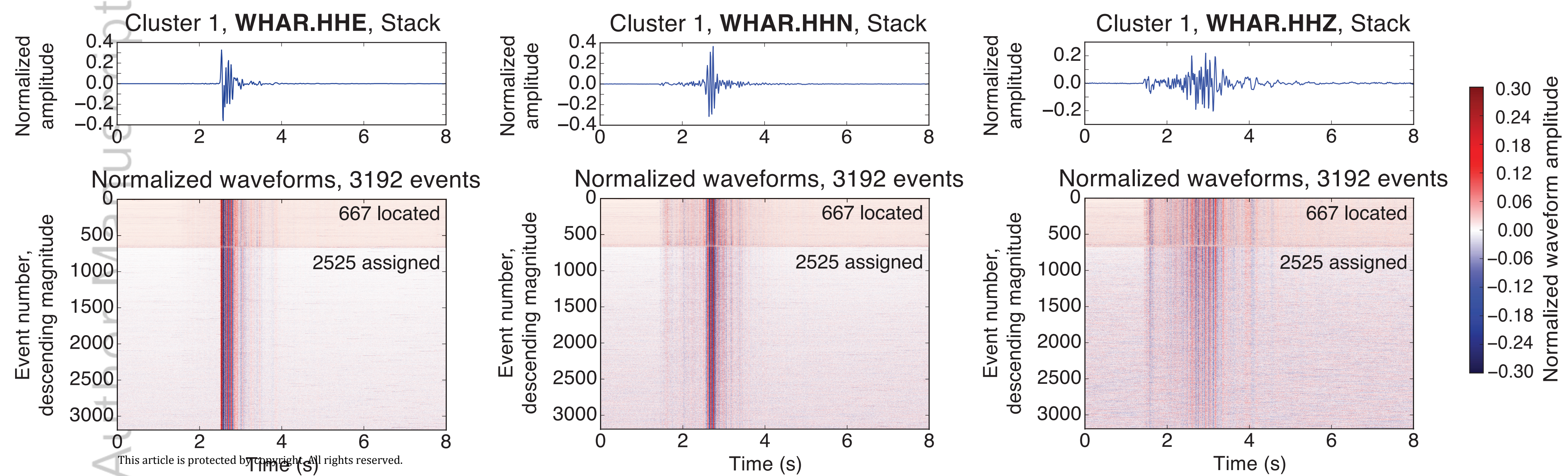


Author Manuscript

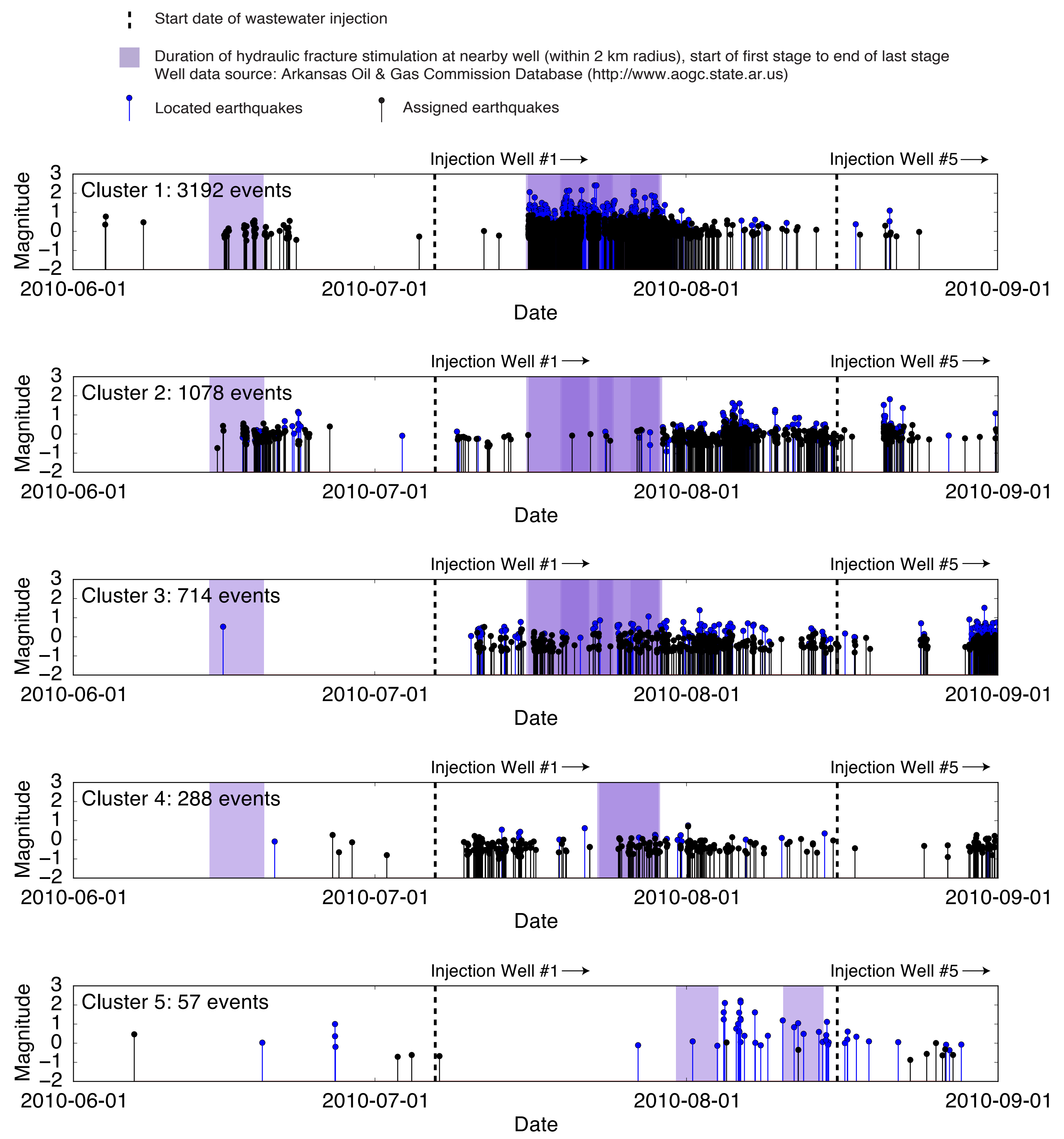
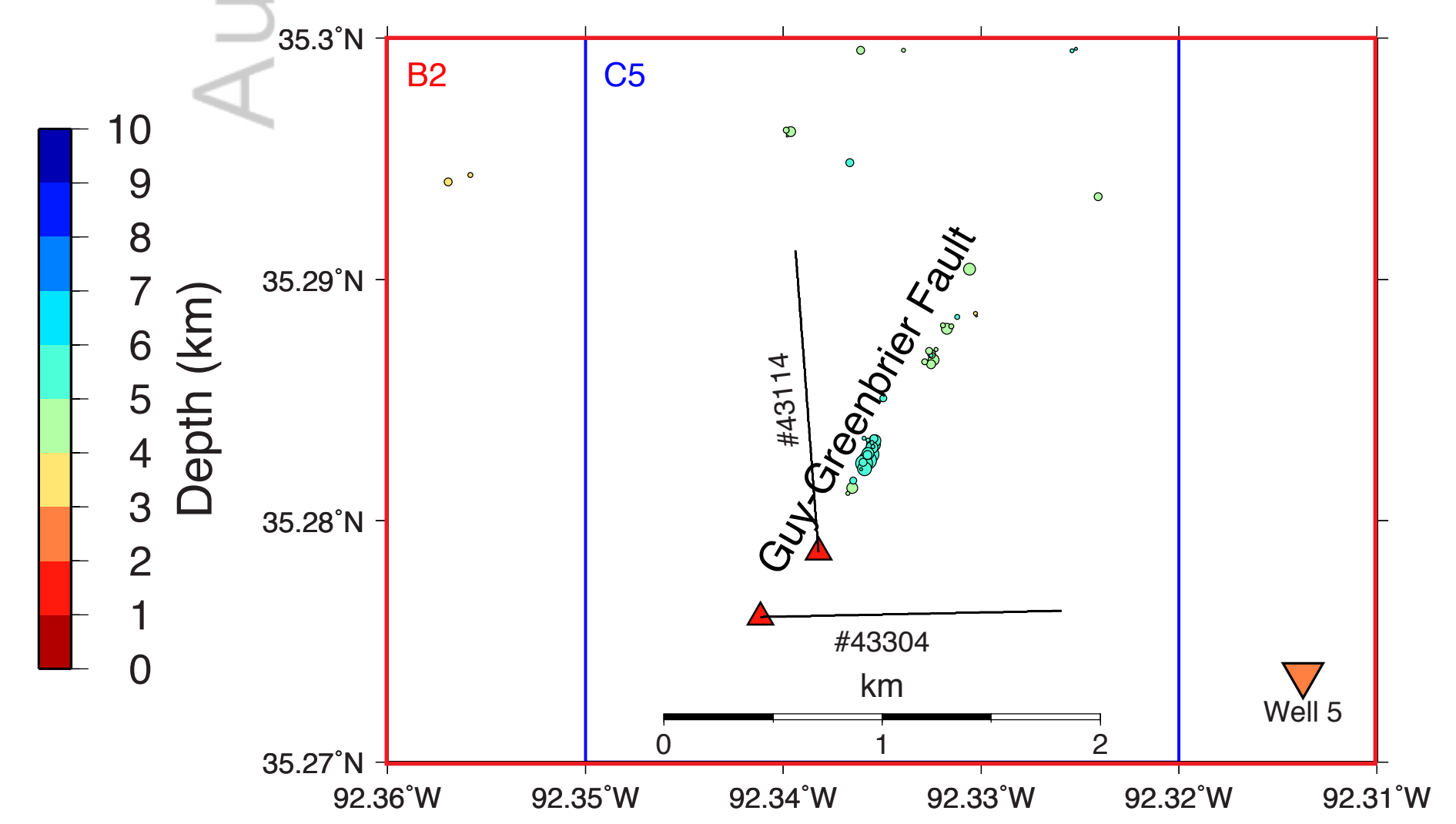
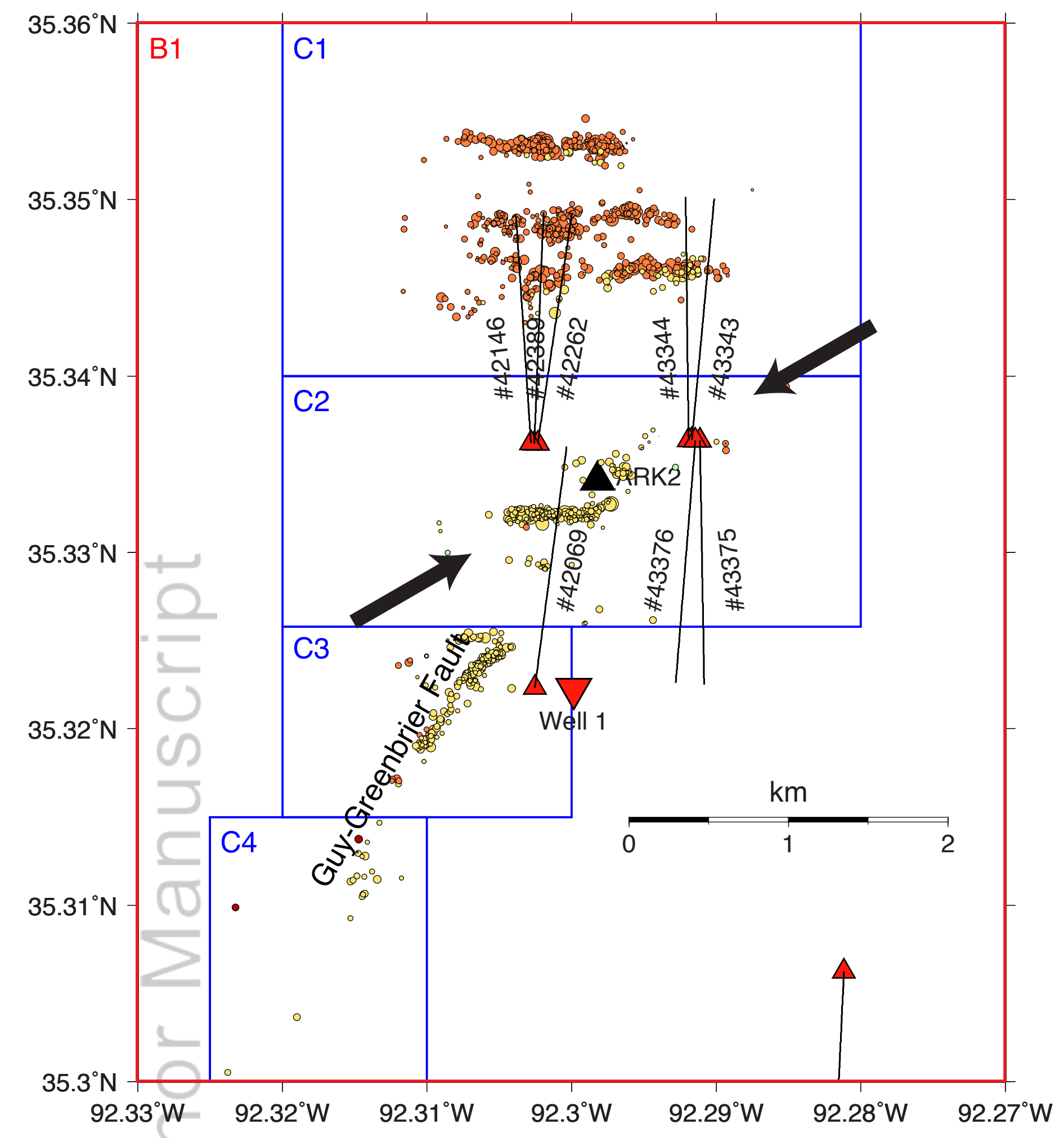
Magnitude-Frequency Distribution



Author Manuscript

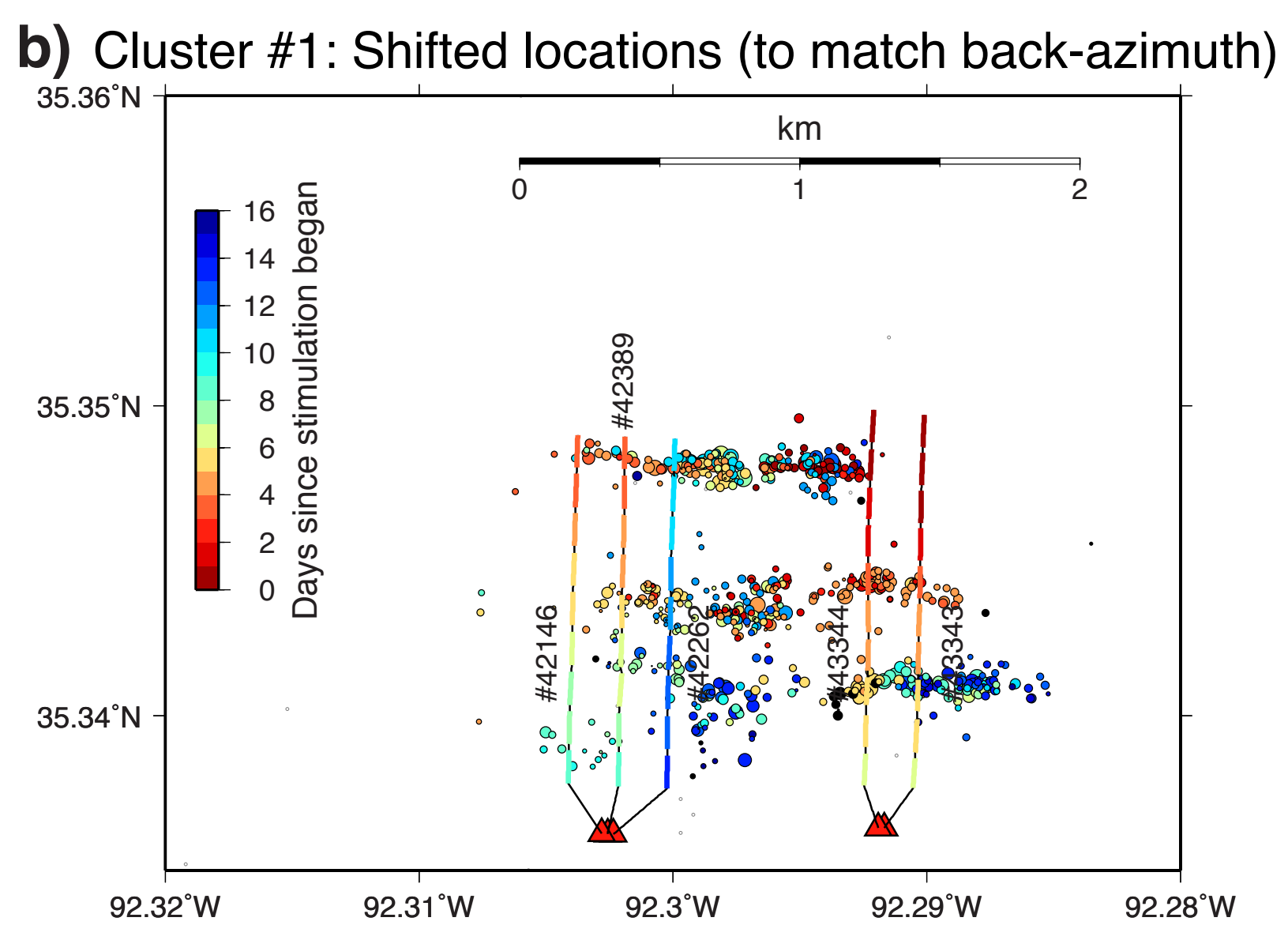
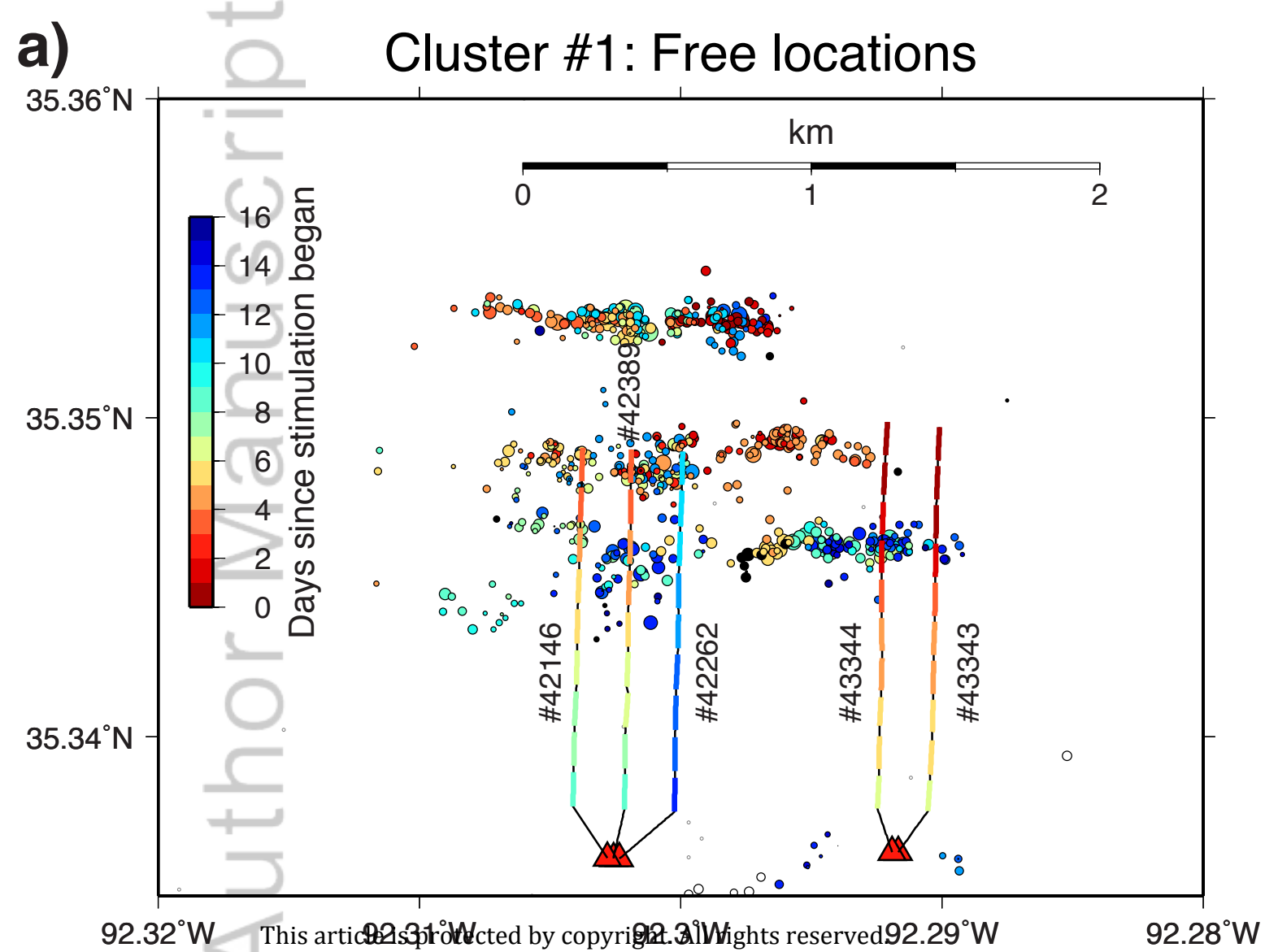


Author Manuscript

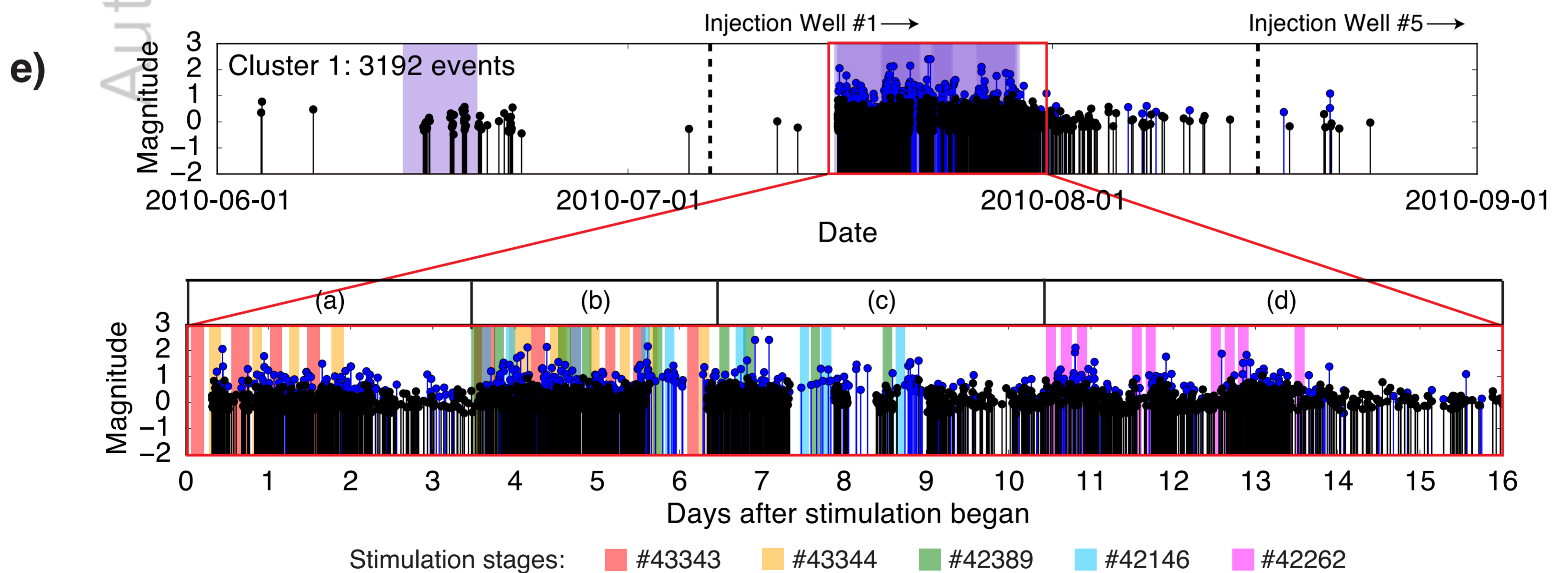
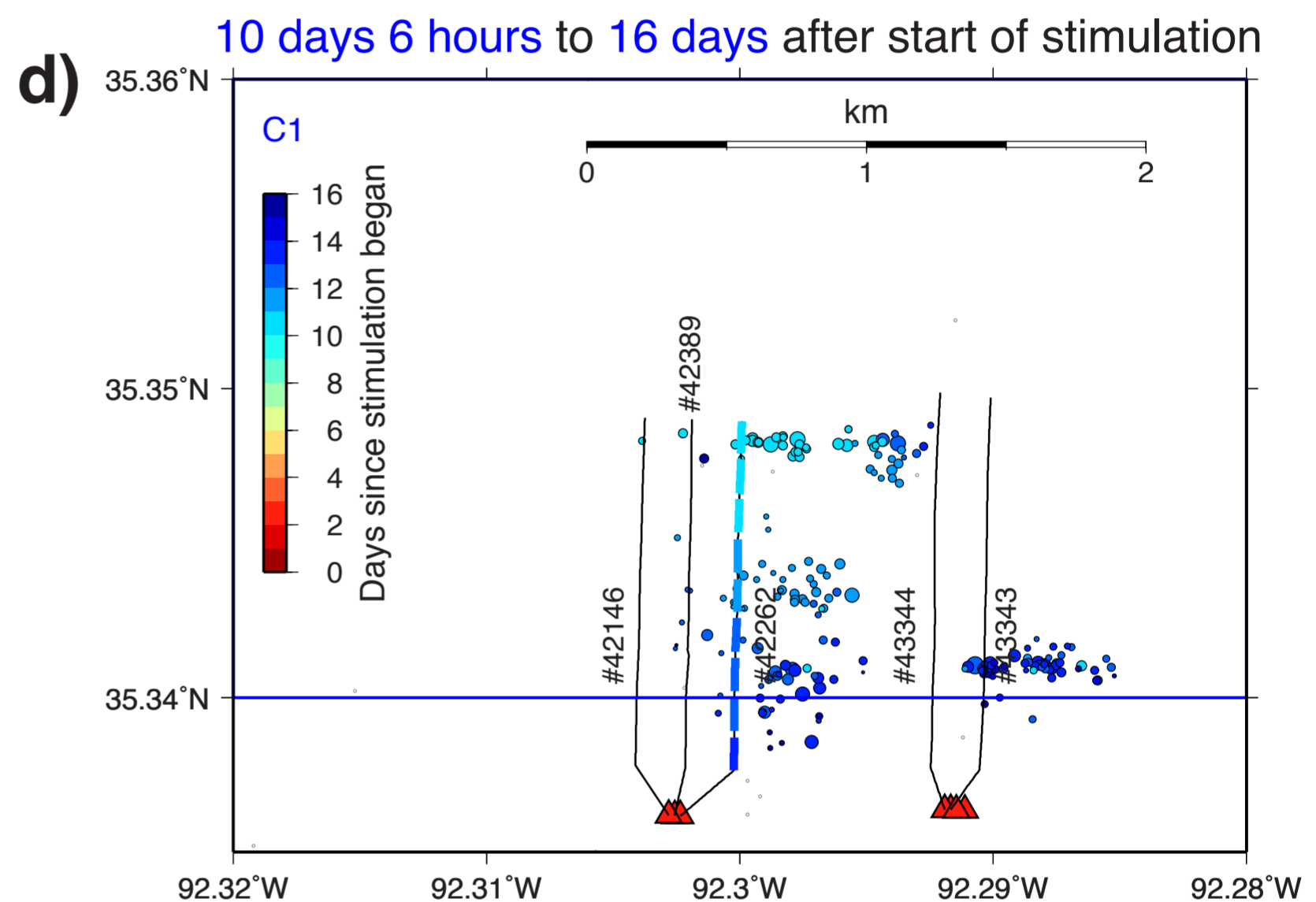
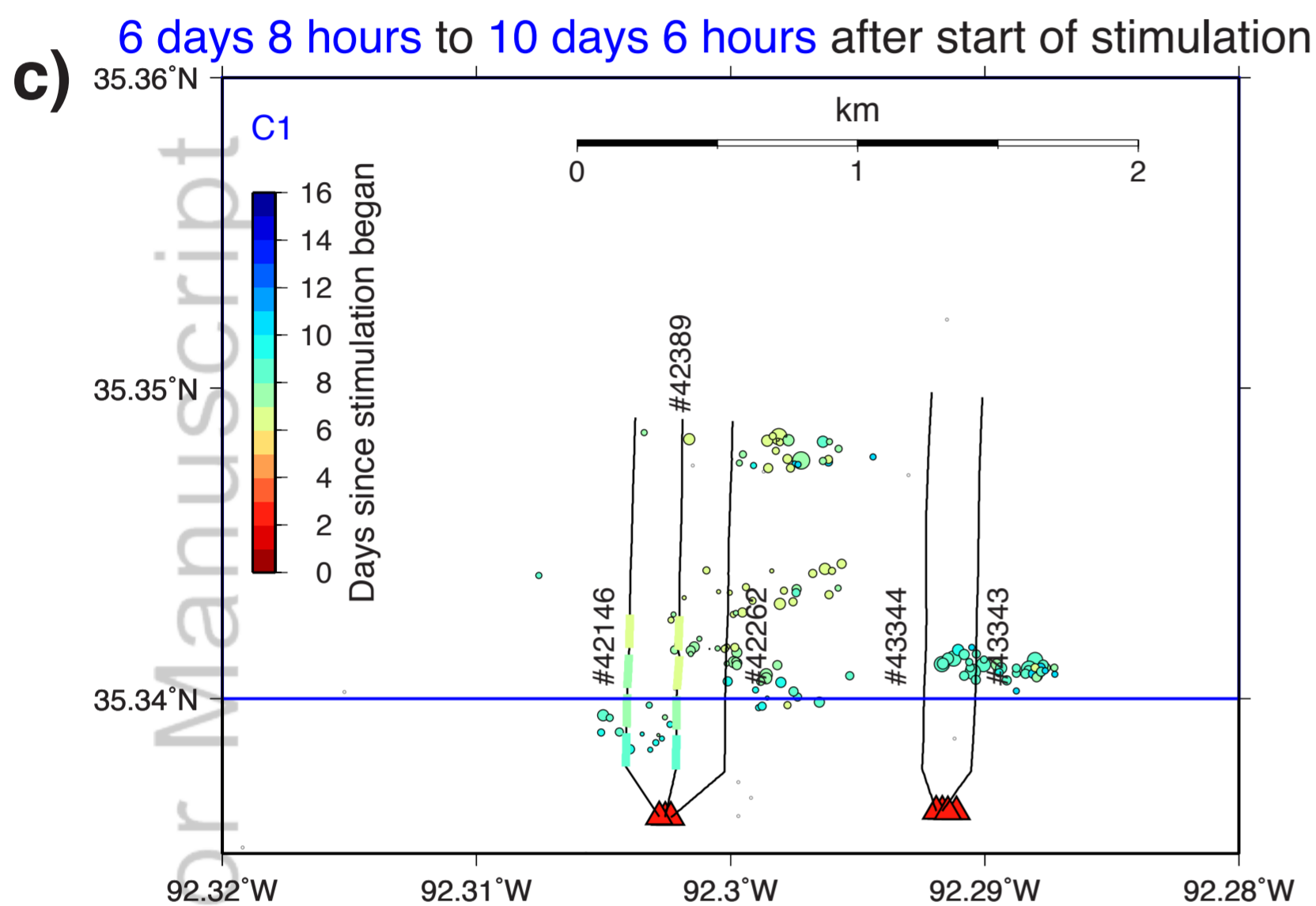
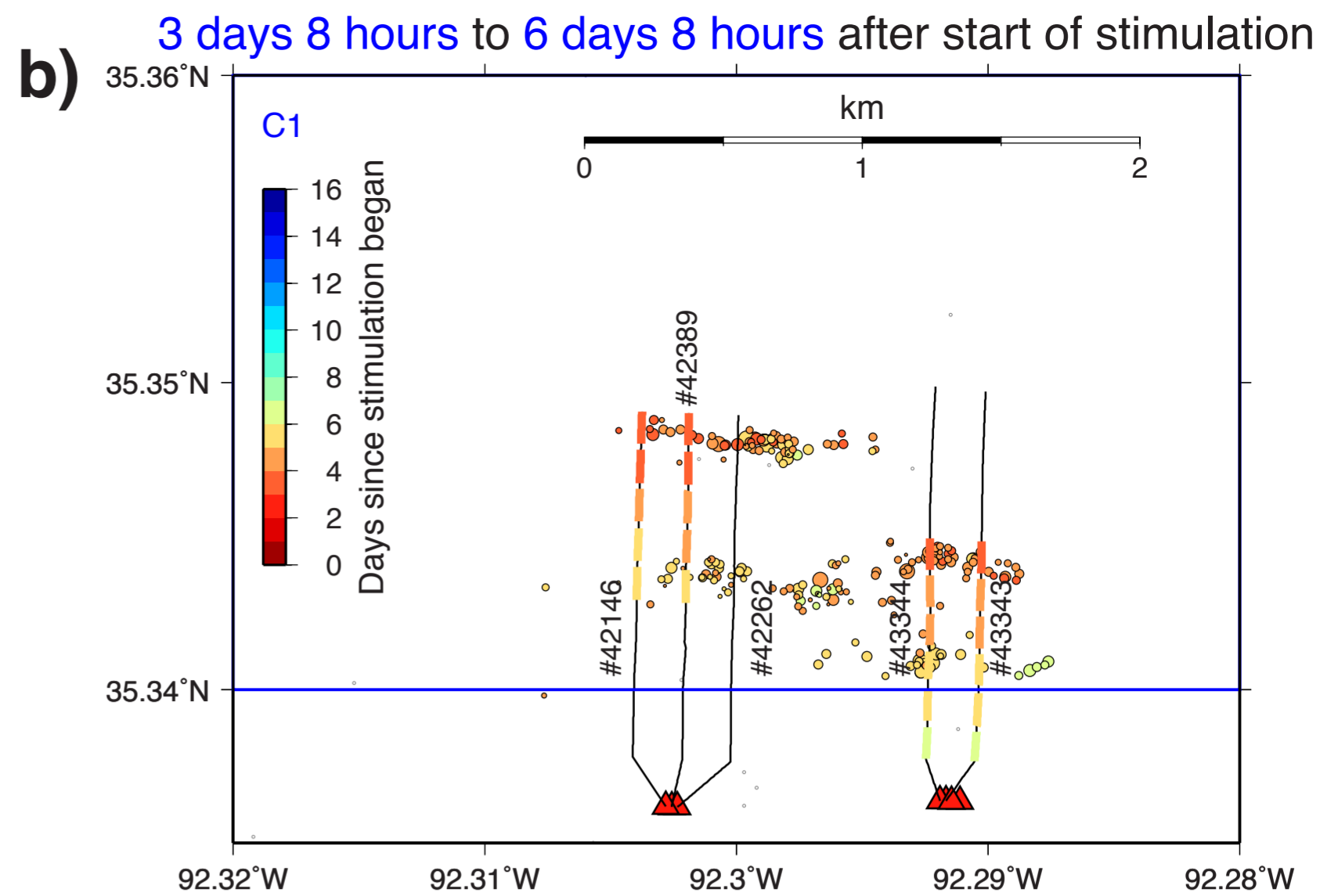
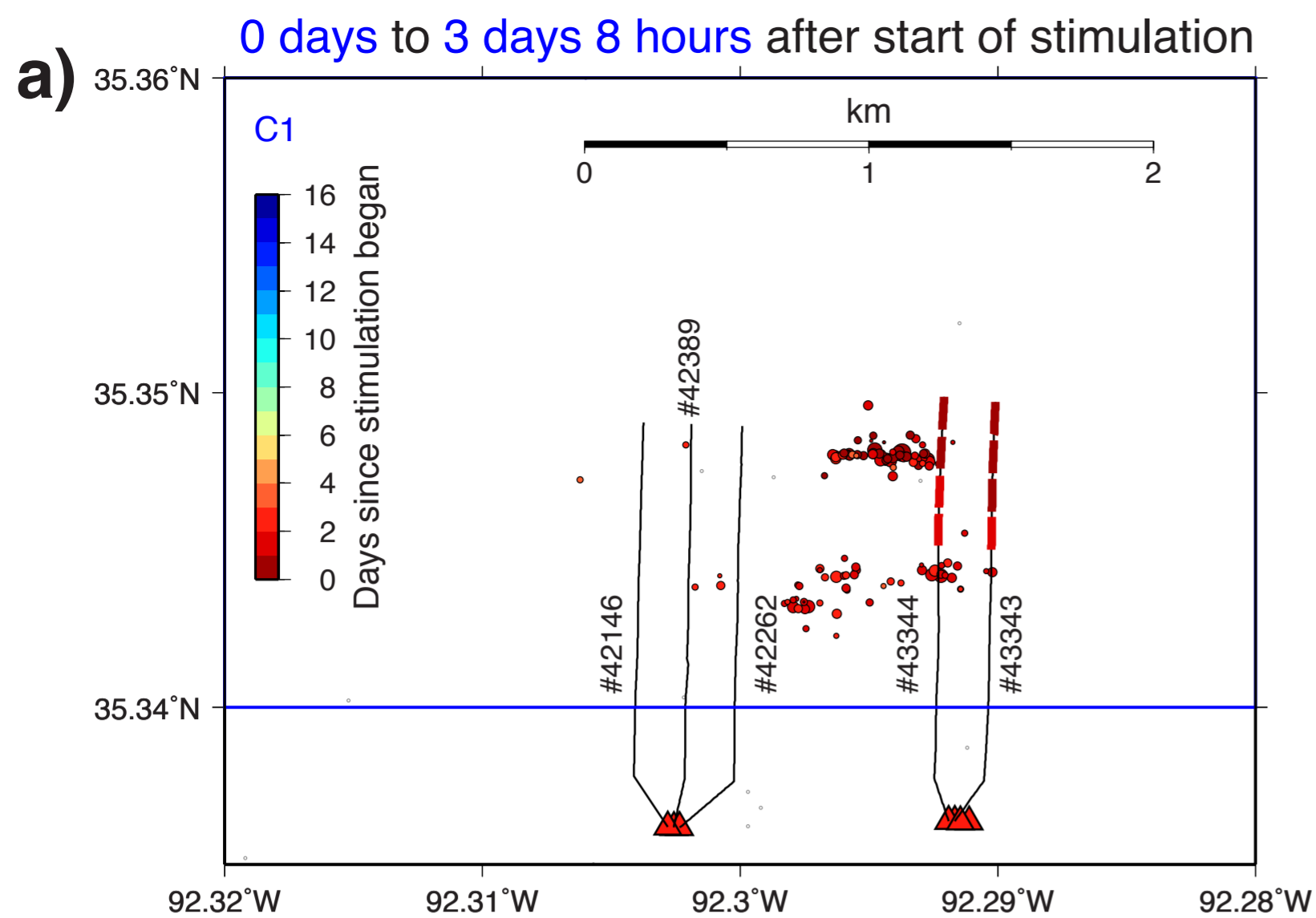


Author Manuscript

Author Manuscript



Author Manuscript



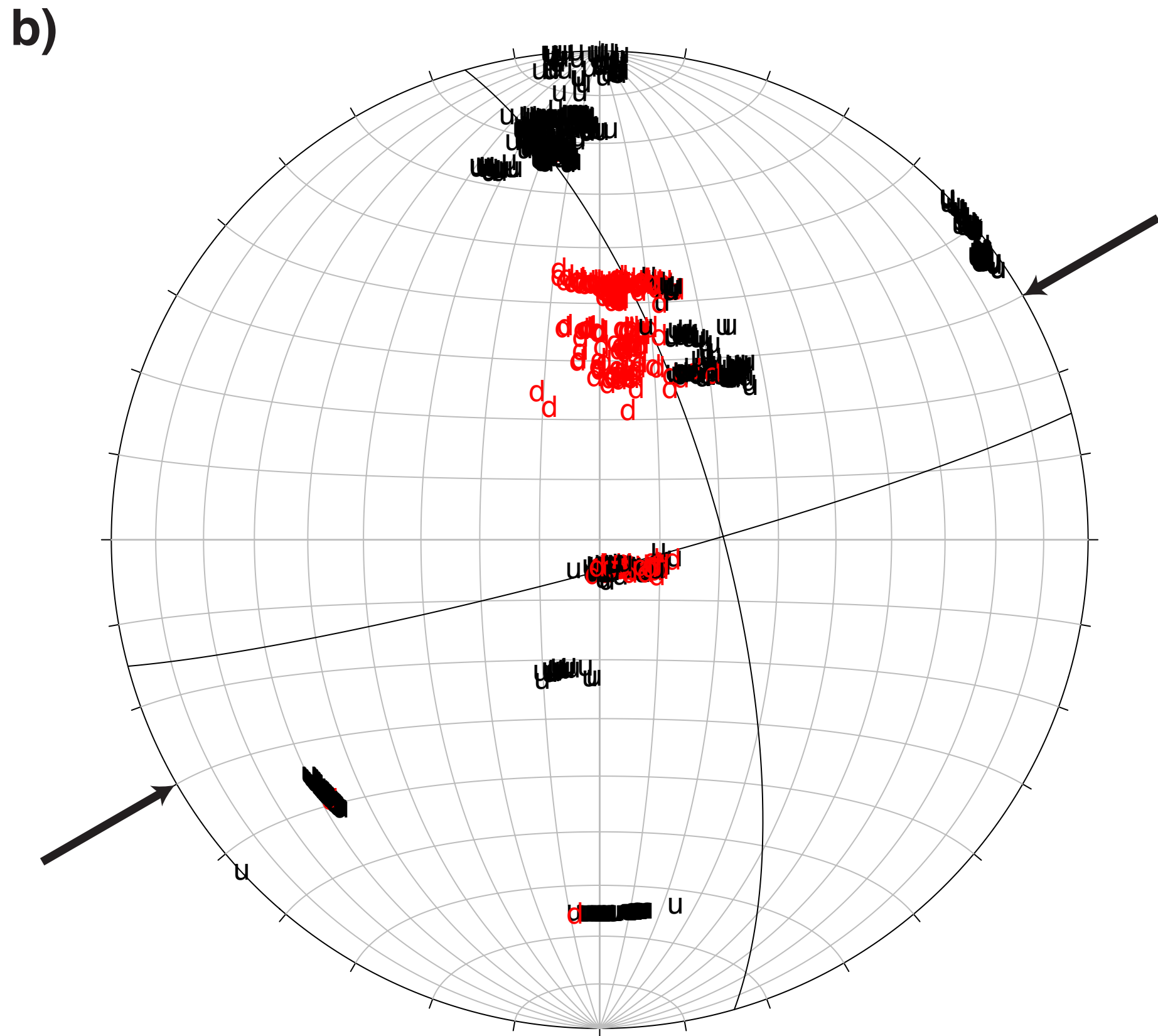
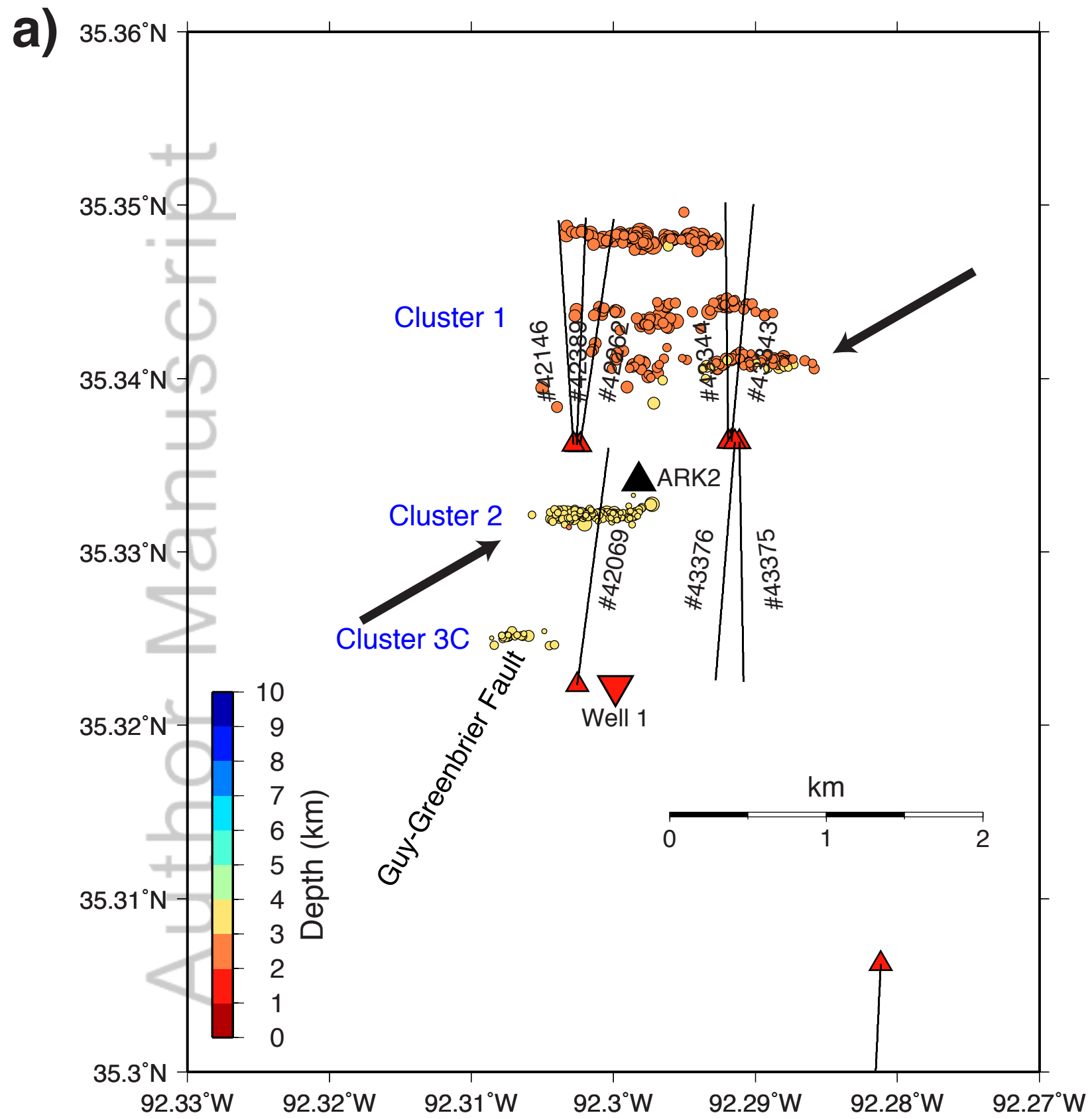
⋮ Start date of wastewater injection

■ Duration of hydraulic fracture stimulation at nearby well (within 2 km radius), start of first stage to end of last stage
Well data source: Arkansas Oil & Gas Commission Database (<http://www.aogc.state.ar.us>)

This article is protected by copyright. All rights reserved.

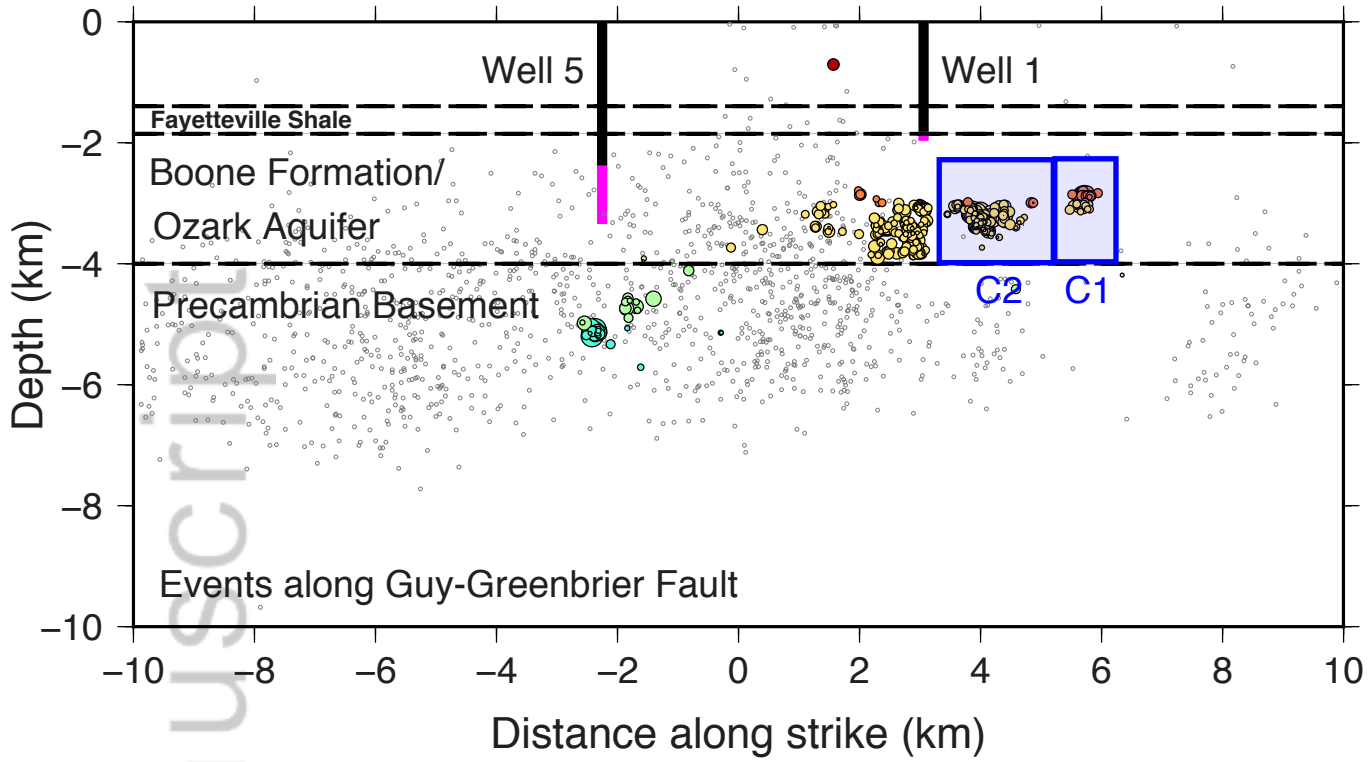
● Located earthquakes
⋮ Assigned earthquakes

Author Manuscript

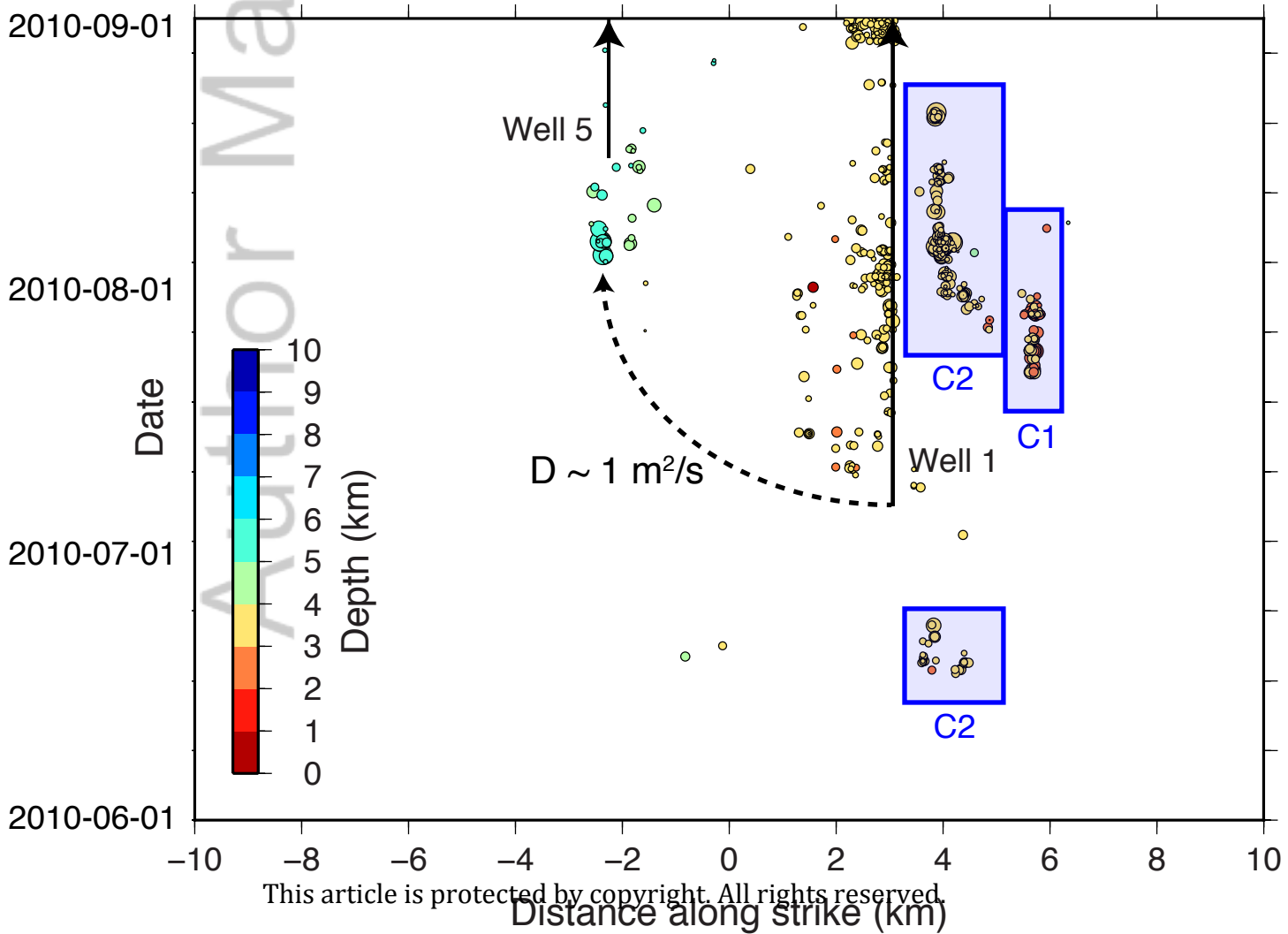


Author Manuscript

a) Profile A–A' along strike of Guy–Greenbrier Fault



b)



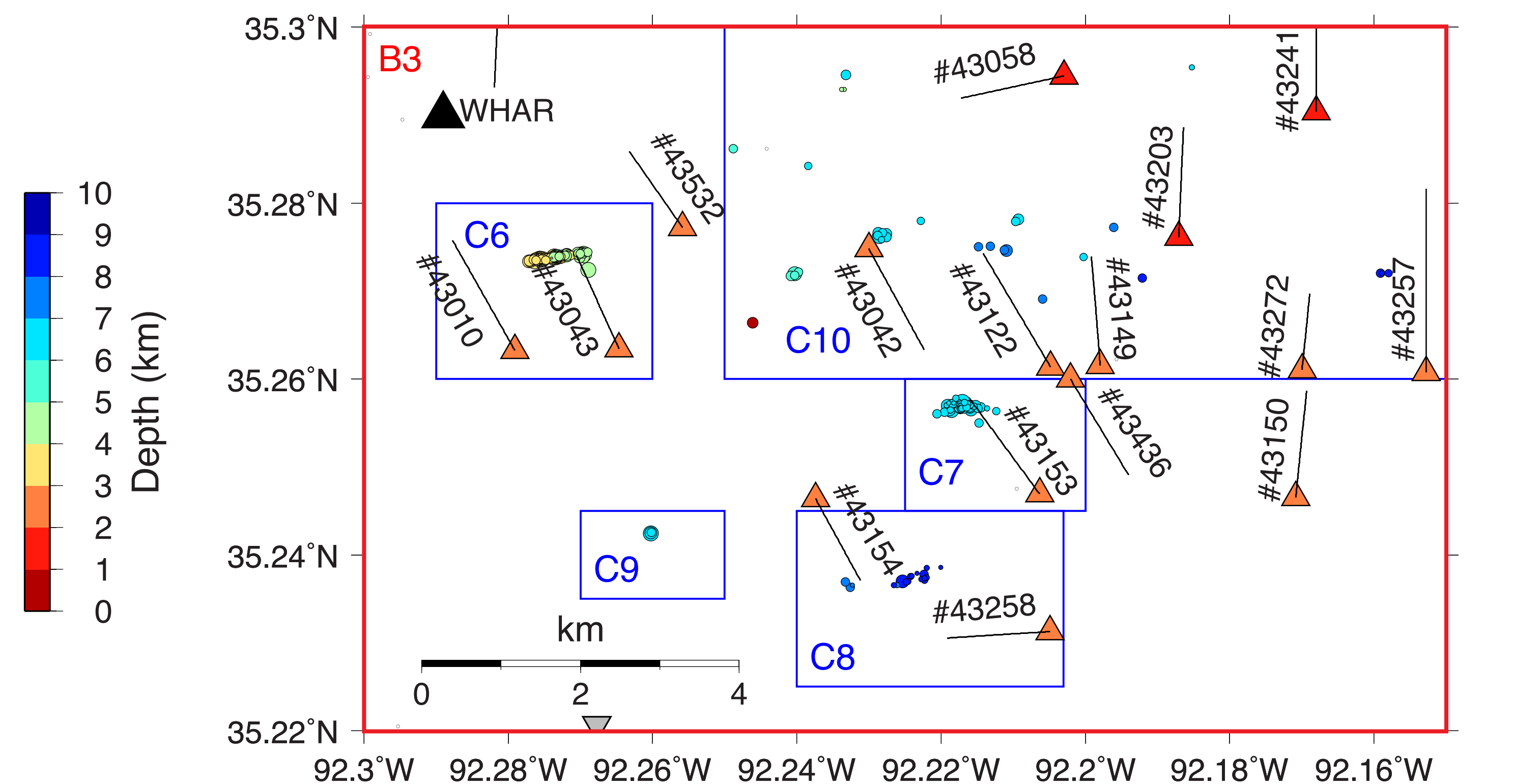
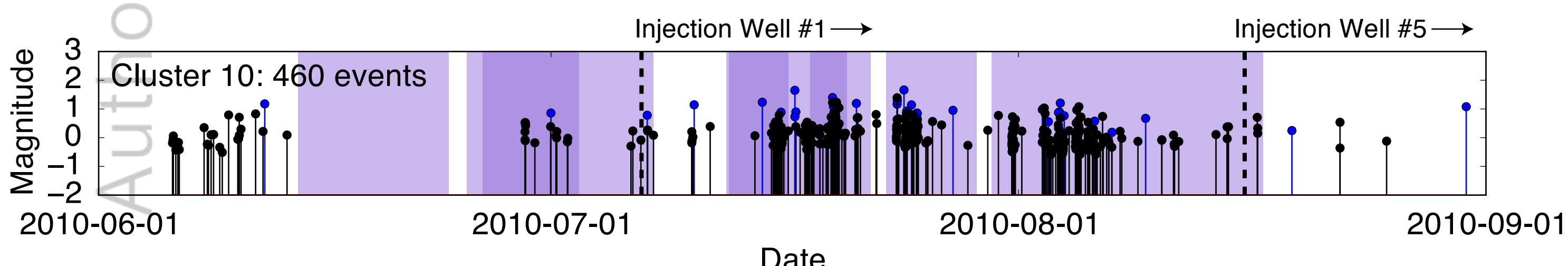
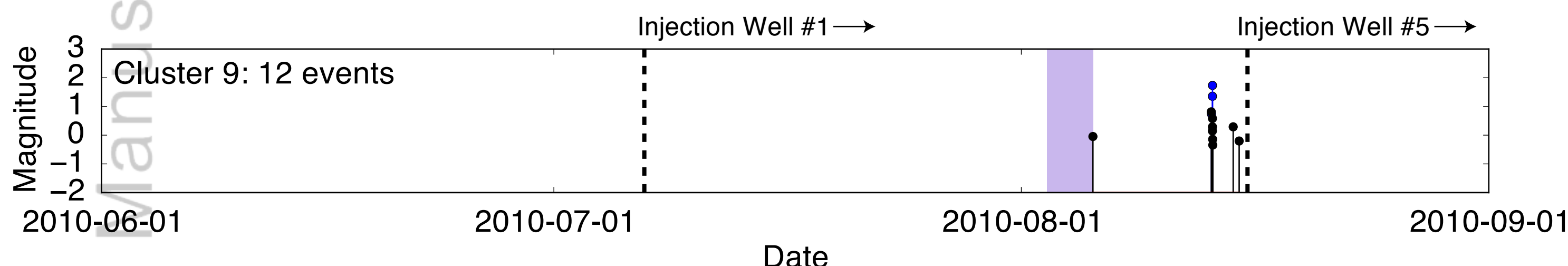
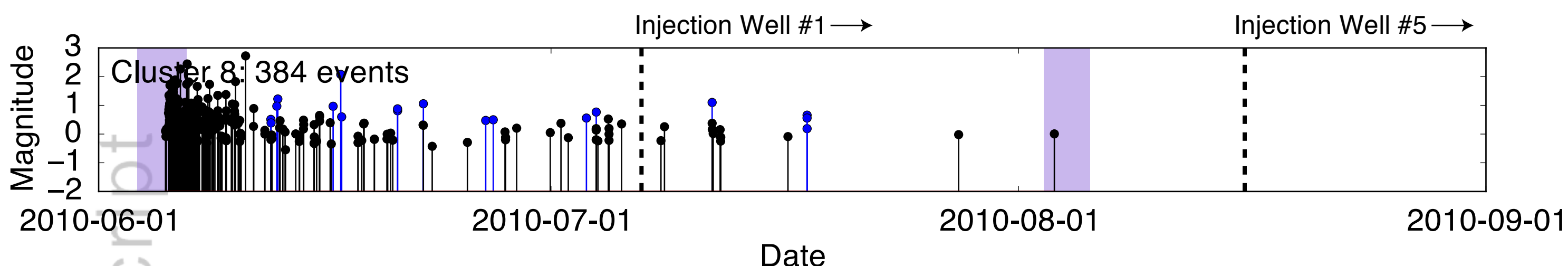
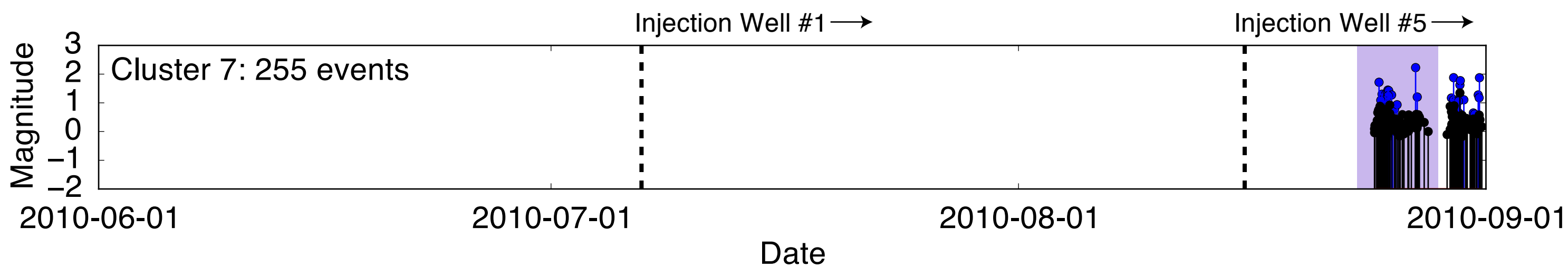
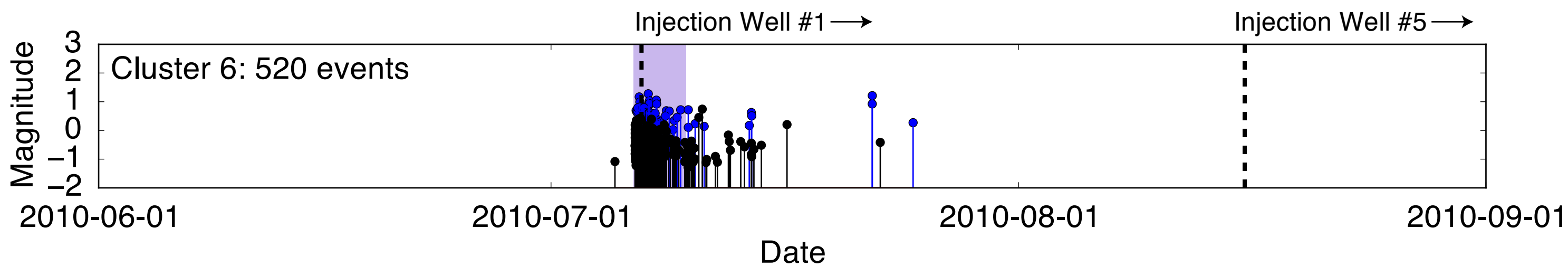
Author Manuscript

Start date of wastewater injection

Duration of hydraulic fracture stimulation at nearby well (within 2 km radius), start of first stage to end of last stage
Well data source: Arkansas Oil & Gas Commission Database (<http://www.aogc.state.ar.us>)

Located earthquakes

Assigned earthquakes



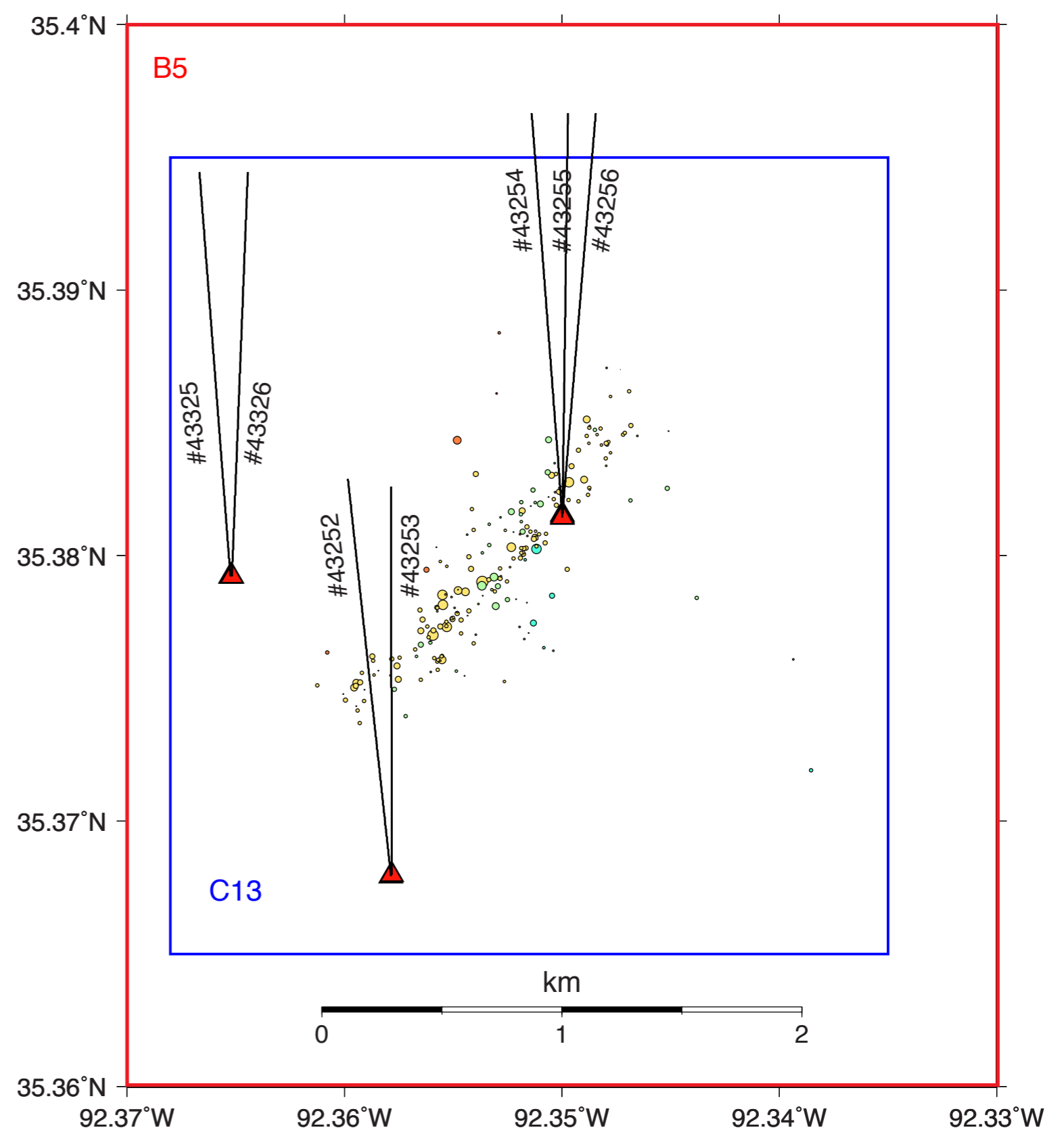
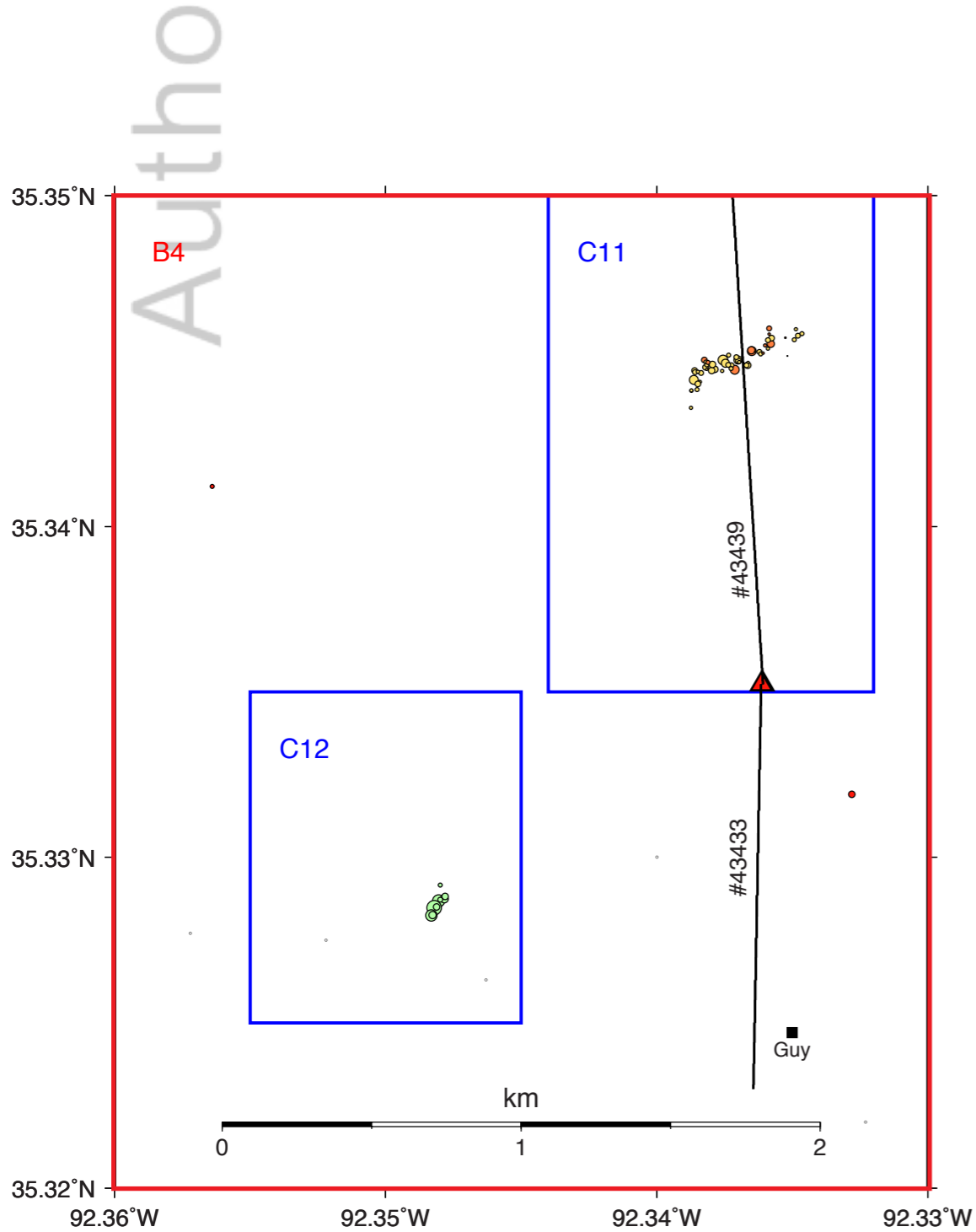
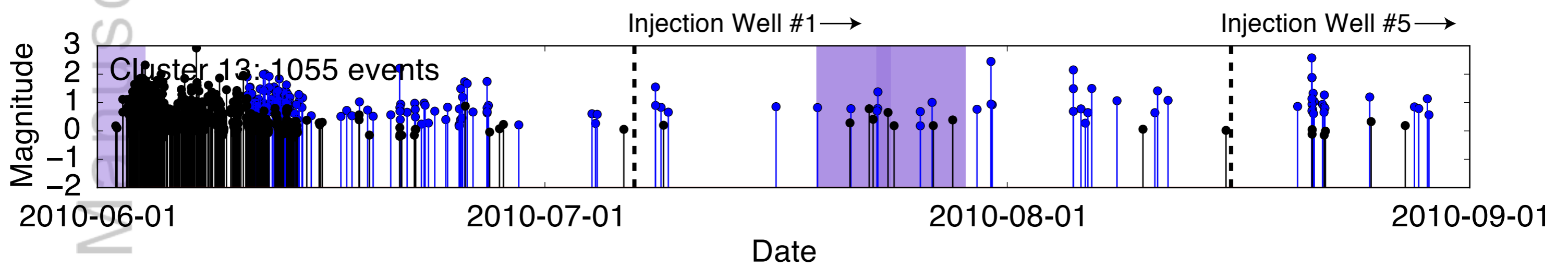
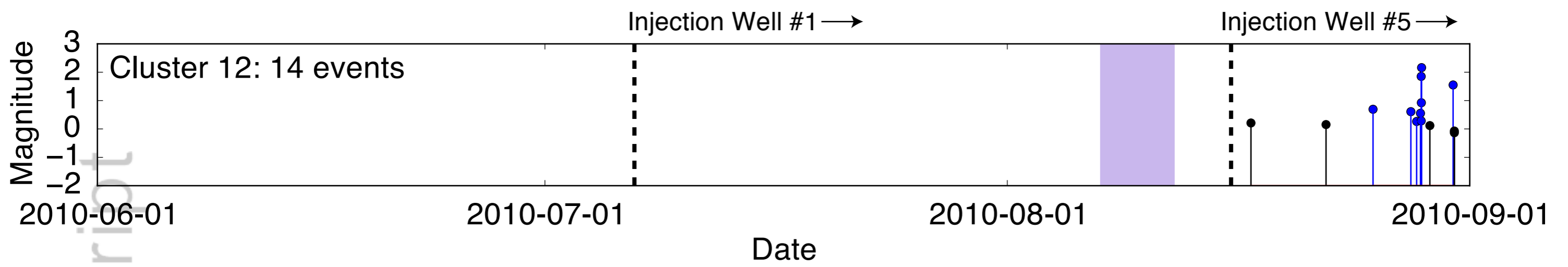
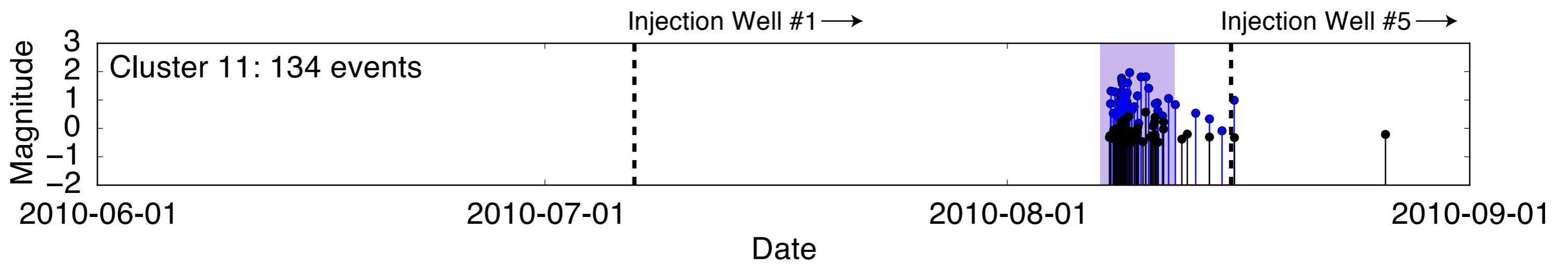
Author Manuscript

┆ Start date of wastewater injection

■ Duration of hydraulic fracture stimulation at nearby well (within 2 km radius), start of first stage to end of last stage
Well data source: Arkansas Oil & Gas Commission Database (<http://www.aogc.state.ar.us>)

● Located earthquakes

● Assigned earthquakes



Author Manuscript

⋮ Start date of wastewater injection

■ Duration of hydraulic fracture stimulation at nearby well (within 2 km radius), start of first stage to end of last stage
Well data source: Arkansas Oil & Gas Commission Database (<http://www.aogc.state.ar.us>)

● Located earthquakes

● Assigned earthquakes

